



Diurnal variability of turbidity and light attenuation in the southern North Sea from the SEVIRI geostationary sensor

G. Neukermans^{a,b,c,d,*}, K.G. Ruddick^a, N. Greenwood^e

^a Management Unit of the North Sea Mathematical Models (MUMM), Royal Belgian Institute for Natural Sciences (RBINS), Gulledele 100, B-1200 Brussels, Belgium

^b Université Lille Nord de France, F-59000 Lille, France

^c Université du Littoral Côte d'Opale (ULCO), Laboratoire d'Océanologie et Géosciences (LOG), F-62930 Wimereux, France

^d Centre National de la Recherche Scientifique (CNRS), UMR 8187, F-62930 Wimereux, France

^e Centre for Environment, Fisheries and Aquaculture Science (Cefas), Pakefield Road, Lowestoft, Suffolk, NR33 0HT, UK

ARTICLE INFO

Article history:

Received 23 November 2011

Received in revised form 10 May 2012

Accepted 3 June 2012

Available online 10 July 2012

Keywords:

PAR attenuation

Atmospheric correction

Tidal variability

Satellite data validation

ABSTRACT

This study follows up on the successful feasibility study of Neukermans et al. (2009) for mapping suspended matter in turbid waters from the SEVIRI sensor on board the METEOSAT geostationary weather satellite platform. Previous methodology is extended to the mapping of turbidity, T , and vertical attenuation of photosynthetically active radiation (PAR), K_{PAR} . The spatial resolution of the SEVIRI products is improved from $3 \text{ km} \times 6.5 \text{ km}$ to $1 \text{ km} \times 2 \text{ km}$ using the broad high resolution visual band. The previous atmospheric correction is further improved and the uncertainties on marine reflectance due to digitization are considered. Based on a two year archive of SEVIRI imagery, available every 15 min, the diurnal variability of T and K_{PAR} is investigated during cloud free periods and validated using half-hourly T and K_{PAR} data obtained from a system of moored buoys (SmartBuoys) in the southern North Sea. Based on numerous match-ups, 80% of SEVIRI derived T and K_{PAR} are within 53% and 39% of SmartBuoy T and K_{PAR} , respectively. Results further show that on cloud free days, the SEVIRI T and K_{PAR} signals are in phase with the SmartBuoy data, with an average difference in the timing of the maximum T and K_{PAR} of 11 min and 23 min, respectively. It is concluded that diurnal variability of T and K_{PAR} can now be mapped by remote sensing offering new opportunities for improving ecosystem models and monitoring of turbidity. Limitations of the current SEVIRI sensor and perspectives for design of future geostationary sensors and synergy with polar orbiting satellites are discussed.

© 2012 Elsevier Inc. All rights reserved.

1. Introduction

Polar-orbiting multispectral ocean colour sensors such as the Sea-viewing Wide Field-of-view Sensor (SeaWiFS), the Moderate Resolution Imaging Spectroradiometer (MODIS), and Medium Resolution Imaging Spectrometer (MERIS) provide 2-day coverage of the global ocean and coastal zones since their respective launches in 1997 and 2002. These sensors have become well-established sources (McClain, 2009) of concentration of chlorophyll a , [Chl a] (see Table 1 for notation), and suspended particulate matter, [SPM], and there has been considerable progress towards many new products including particulate and dissolved organic and inorganic carbon (Stramski et al., 1999; Vantrepotte et al., 2011), particle size distribution (Loisel et al., 2006), phytoplankton species composition (Alvain et al., 2008), vertical light attenuation (Stumpf et al., 1999), turbidity (Nechad et al., 2009; Stumpf et al., 1999; Woodruff et al., 1999) etc. During the last decades

the spectral and spatial resolution of space-borne ocean colour sensors has improved, from multispectral to hyperspectral (e.g., Hyperspectral Imager for the Coastal Ocean, launched in September 2009), and from 1 km nadir pixel resolution down to less than 100 m in coastal areas. The quality and quantity of atmospheric corrections and bio-optical algorithms has also significantly progressed.

Even though further progress can still be expected for polar-orbiting sensors in terms of sensor design and processing algorithms, their sampling frequency, typically once per day, is insufficient for many studies and applications. Many physical and biogeochemical processes in coastal regions show variability at time scales shorter than the daily sampling frequency of polar-orbiting sensors. For example, in situ measurements have shown that [SPM] can vary by a factor two or more during the day due to horizontal advection and/or vertical resuspension forced by tides or wind events (Eisma & Irion, 1988; Thompson et al., 2011). Hence, long term data series from polar-orbiting sensors are affected by aliasing that can only be treated indirectly (e.g., Stumpf et al., 1993). Furthermore, cloudiness and/or sun glint reduce data availability from typically once per day (e.g. mid-latitude MODIS imagery) to significantly less. Remote sensing applications, such as harmful algae bloom detection (Stumpf et al., 2003; Tomlinson et al., 2004), have critical vulnerability to such data gaps.

* Corresponding author at: Marine Physical Laboratory, Scripps Institution of Oceanography, University of California, San Diego, La Jolla, CA 92093-0238, USA. Tel.: +1 858 534 7841. Fax: +1 858 534 7641.

E-mail addresses: gneukermans@ucsd.edu (G. Neukermans), k.ruddick@mumm.ac.be (K.G. Ruddick), naomi.greenwood@cefas.co.uk (N. Greenwood).

Table 1
Notation.

Symbol	Parameter definition, units
A_0	SEVIRI solar channel calibration correction factor, dimensionless
A_S, A_T	[SPM] and turbidity retrieval algorithm calibration constants, mg L^{-1} or FNU
B_S, B_T	[SPM] and turbidity retrieval algorithm offsets, mg L^{-1} or FNU
b_b, b_{bp}, b_{bw}	Total, particulate, and pure water backscattering coefficient, m^{-1}
b_{bp}^m	b_{bp} -[SPM], mass-specific backscattering coefficient, $\text{m}^2 \text{g}^{-1}$
[Chl a]	Chlorophyll a pigment concentration, $\mu\text{g L}^{-1}$
c_f	Calibration gain factor for SEVIRI bands, $\text{mW m}^{-2} \text{sr}^{-1} \text{cm}$
Δ	Uncertainty of a measurement
Δ_a	Aerosol correction uncertainty, dimensionless
Δ_d	Digitization uncertainty, dimensionless
Δ_w	Turbid water uncertainty, dimensionless
ε	VIS06:VIS08 band ratio of aerosol reflectances, dimensionless
E_d	Downwelling spectral irradiance, $\text{W m}^{-2} \text{nm}^{-1}$
E_0^{TOA}	Extraterrestrial solar irradiance at TOA, $\text{W m}^{-2} \mu\text{m}^{-1}$
ϕ, ϕ_v, ϕ_0	Azimuth angle, sensor and sun azimuth angle
γ	VIS06:VIS08 ratio of two-way aerosol transmittances, dimensionless
K_d	Spectral diffuse attenuation coefficient for downwelling irradiance, m^{-1}
$K_{\text{PAR}}^{\text{SB}}$	Vertical attenuation of PAR derived from SmartBuoy PAR data, m^{-1}
$K_{\text{PAR}, \otimes}$	Vertical attenuation of PAR derived from SEVIRI on the HRV grid, m^{-1}
K_{PAR}	Diffuse attenuation coefficient of PAR, m^{-1}
\bar{K}_{PAR}	Vertically averaged diffuse attenuation coefficient of PAR, m^{-1}
λ	Wavelength of light, nm or μm
λ_0	Waveband central wavelength, nm or μm
I_a^{TOA}	Aerosol radiance at TOA, $\text{W m}^{-2} \text{sr}^{-1} \mu\text{m}^{-1}$
I_g^{TOA}	Sun glint radiance at TOA, $\text{W m}^{-2} \text{sr}^{-1} \mu\text{m}^{-1}$
I_r^{TOA}	Rayleigh (air molecule) radiance at TOA, $\text{W m}^{-2} \text{sr}^{-1} \mu\text{m}^{-1}$
I_{ra}^{TOA}	Aerosol-Rayleigh multiple scattering radiance at TOA, $\text{W m}^{-2} \text{sr}^{-1} \mu\text{m}^{-1}$
$I_{\text{tot}}^{\text{TOA}}$	Total radiance at TOA, $\text{W m}^{-2} \text{sr}^{-1} \mu\text{m}^{-1}$
$L_w^{\text{TOA}}, L_w^{0+}$	Water-leaving radiance at TOA or above-water, $\text{W m}^{-2} \text{sr}^{-1} \mu\text{m}^{-1}$
$L_{\text{wc}}^{\text{TOA}}$	White-cap radiance at TOA, $\text{W m}^{-2} \text{sr}^{-1} \mu\text{m}^{-1}$
m	Two-way air mass, dimensionless
n_o	Total number of observations
n_x	Number of outliers
$\omega(\lambda)$	Sensor spectral response function, dimensionless
PAR	Photosynthetically active radiation, $\text{photons s}^{-1} \text{m}^{-2}$
r	Correlation coefficient, dimensionless
r_0	Calibration offset factor for SEVIRI bands, $\text{mW m}^{-2} \text{sr}^{-1} \text{cm}$
ρ	Reflectance, dimensionless
$\bar{\rho}$	Spatial average of the HRV reflectance on the VIS06 grid, dimensionless
$\hat{\rho}$	Spatial anomaly of the HRV reflectance within the VIS06 grid, dimensionless
ρ_a^{TOA}	Aerosol reflectance at TOA, dimensionless
ρ_c	Rayleigh and gas corrected reflectance at TOA, dimensionless
ρ_g^{TOA}	Sun glint reflectance at TOA, dimensionless
ρ_{ra}^{TOA}	Rayleigh-aerosol interaction reflectance at TOA, dimensionless
$\rho_{\text{tot}}^{\text{TOA}}$	Total reflectance at TOA, dimensionless
ρ_w^{TOA}	Marine reflectance at TOA, dimensionless
ρ_w^{0+}	Above-water marine reflectance, dimensionless
$\rho_w^{0+, \otimes}$	Above-water marine reflectance on HRV grid, dimensionless
$\rho_{\text{wc}}^{\text{TOA}}$	White cap reflectance at TOA, dimensionless
σ	VIS06:VIS08 band ratio of marine reflectance (dimensionless), or standard deviation, depending on the context
[SPM]	Suspended particulate matter concentration, g m^{-3}
$t_o^a, t_v^a, t_{o,v}^a$	Sun-sea, sea-sensor, and two-way aerosol transmittance, dimensionless
$t_o^g, t_v^g, t_{o,v}^g$	Sun-sea, sea-sensor, and two-way atmospheric gas transmittance, dimensionless
$t_o^r, t_v^r, t_{o,v}^r$	Sun-sea, sea-sensor, and two-way Rayleigh transmittance, dimensionless
T	Turbidity, FNU
$T_0, T_v, T_{o,v}$	Total sun-sea, sea-sensor, and two-way atmospheric transmittance, dimensionless
τ^{SB}	Turbidity recorded by SmartBuoy, m^{-1}
T_{\otimes}	Turbidity retrieved by SEVIRI on the HRV grid, FNU
θ_v	Viewing zenith angle, degrees
θ_0	Solar zenith angle, degrees

Ocean colour remote sensing from geostationary sensors has the potential to overcome or mitigate these limitations: the availability of ocean colour data would significantly increase during periods of scattered clouds (Mazeran & Meskini, 2008) and the much higher sampling frequency, typically 1 per hour or higher, allows to observe the diurnal or tidal cycles of optical and biogeochemical processes of the open ocean and coastal waters. Geostationary ocean colour data offers possibilities to study the coupling between physics and biogeochemistry, to quantify fluxes and study transport of carbon and sediment. Assimilation of geostationary ocean colour data into ecosystem models may improve modelling results and eutrophication studies. For example, the availability of light to marine organisms may vary rapidly in coastal environments due to rapid changes in water turbidity. In light-limited ecosystems such as the Channel and Southern Bight of the North Sea, this unrepresented high frequency variability of underwater light may be a cause of discrepancy between the modelled and observed timing of the phytoplankton spring bloom (Lacroix et al., 2007).

The Geostationary Ocean Colour Imager (GOCI, Faure et al., 2008), launched by the Korean Space Agency (KORDI) in June 2010, is the first ocean colour sensor in geostationary orbit. It provides hourly multispectral imagery of waters surrounding the Korean peninsula at a spatial resolution of 500 m. Other national and international space agencies have plans to launch geostationary ocean colour sensors. The European Space Agency (ESA) has commissioned studies on user requirements and some concept design in the framework of Geo-Oculus. A proposal to host a GOCI-like sensor on a geostationary telecommunication satellite has been submitted to ESA (Antoine et al., 2011). The Hosted Ocean Colour Imager, HOCI, would provide hourly multi-spectral imagery of the European seas and adjacent open ocean from late 2014. NASA is preparing the Geostationary Coastal Ocean and Air Pollution Events (GEO-CAPE) mission, planned to be operational by 2020 (NRC, 2007).

Even though the Spinning Enhanced Visible and Infrared Imager (SEVIRI) radiometer onboard the METEOSAT Second Generation (MSG) satellite platform is not capable of ocean colour remote sensing because of its limited spectral resolution, SEVIRI has sufficient bands for the mapping of [SPM] in turbid waters (Neukermans et al., 2009). SEVIRI imagery, available since 2004 at 15 minute temporal resolution, offers the possibility to address the problems (reduced signal at high orbit and high viewing zenith) and advantages (high temporal resolution, stable viewing geometry) specific to the geostationary orbit. The feasibility study for mapping [SPM] with SEVIRI (Neukermans et al., 2009) was a first attempt to exploit the potential of a geostationary platform for marine optics. This study, based on a one month SEVIRI dataset of the southern North Sea, has shown that [SPM] can be reliably detected in turbid waters, but with considerable uncertainties in clear waters due to SEVIRI's low radiometric resolution. Even though at a much lower spatial resolution ($3 \text{ km} \times 6.5 \text{ km}$), SEVIRI [SPM] products were shown to correlate well with MODIS-AQUA 667 nm [SPM] products, and SEVIRI's marine reflectance correlated well with marine reflectance from the spectrally similar MODIS-AQUA 645 nm band (Neukermans, 2012).

The present study follows up on the successful feasibility study of Neukermans et al. (2009). The specific objectives of this study are to (i) improve the spatial resolution of SEVIRI products using its High Resolution Visual (HRV) band, (ii) improve the quality of the existing atmospheric correction and extend its uncertainty estimation to include digitization effects, (iii) extend the methodology to the mapping of turbidity, T , and vertical attenuation of photosynthetically active radiation (PAR), K_{PAR} , with uncertainty estimates, (iv) investigate diurnal variability of T and K_{PAR} during cloud free periods based on a two year SEVIRI archive, and (v) validate SEVIRI T and K_{PAR} products and their temporal dynamics using T and K_{PAR} data obtained from a system of moored buoys in the southern North Sea.

2. Materials and methods

The necessary definitions and notation are introduced to describe the use of the HRV band to improve the spatial resolution of the marine reflectance product. Next, improvements to the atmospheric correction of Neukermans et al. (2009) are described and uncertainties on marine reflectance products are given in Section 2.4. Algorithms for the retrieval of T and K_{PAR} are presented and the uncertainty on each product is assessed in Sections 2.5 and 2.6, respectively. Finally, validation of SEVIRI products and diurnal variability is described.

2.1. Definitions

At a wavelength λ , the total radiance at the top-of-atmosphere (TOA) sensed by a satellite sensor can be decomposed as follows:

$$L_{tot}^{TOA}(\lambda) = L_r^{TOA}(\lambda) + L_a^{TOA}(\lambda) + T_v(\lambda)L_w^{0+}(\lambda) \quad (1)$$

where L_{tot}^{TOA} , L_r^{TOA} and L_a^{TOA} are the wavelength dependent total, Rayleigh (due to air molecules) and aerosol radiances at TOA (units: $W m^{-2} sr^{-1} \mu m^{-1}$). $L_w^{0+}(\lambda)$ is the upwelling radiance just above the sea surface and $T_v(\lambda)$ is the sea-sensor atmospheric transmittance due to air molecules (t_v^a), aerosols (t_v^a), and atmospheric gasses (t_v^g):

$$T_v(\lambda) = t_v^r(\lambda)t_v^a(\lambda)t_v^g(\lambda) = \frac{L_w^{TOA}(\lambda)}{L_w^{0+}(\lambda)} \quad (2)$$

For a spectral band B with spectral response function $\omega(\lambda)$, spectral integration of Eq. 1 gives:

$$\int \omega(\lambda)L_{tot}^{TOA}(\lambda)d\lambda = \int \omega(\lambda)L_r^{TOA}(\lambda)d\lambda + \int \omega(\lambda)L_a^{TOA}(\lambda)d\lambda + \int \omega(\lambda)T_v(\lambda)L_w^{0+}(\lambda)d\lambda \quad (3)$$

The band-integrated total, Rayleigh, and aerosol reflectance at TOA are obtained through normalization of their respective band-integrated irradiances at TOA by $\int \omega(\lambda)E_d^{TOA}(\lambda)d\lambda$, where $E_d^{TOA}(\lambda)$ is the downwelling irradiance at TOA (units: $W m^{-2} \mu m^{-1}$). Thus:

$$\rho_{tot}^{TOA(B)} = \pi \frac{\int \omega(\lambda)L_{tot}^{TOA}(\lambda)d\lambda}{\int \omega(\lambda)E_d^{TOA}(\lambda)d\lambda} \quad (4)$$

which can be written analogously for $\rho_r^{TOA(B)}$, $\rho_a^{TOA(B)}$ and $\rho_w^{TOA(B)}$. This gives the decomposition of total reflectance at TOA for band B :

$$\rho_{tot}^{TOA(B)} = \rho_r^{TOA(B)} + \rho_a^{TOA(B)} + \rho_w^{TOA(B)} \quad (5)$$

The above-water marine reflectance, $\rho_w^{0+}(\lambda)$, is defined as:

$$\rho_w^{0+}(\lambda) = \pi \frac{L_w^{0+}(\lambda)}{E_d^{0+}(\lambda)} \quad (6)$$

where $E_d^{0+}(\lambda)$ is the above-water downwelling irradiance, which is related to $E_d^{TOA}(\lambda)$ via the total atmospheric transmittance from sun to sea:

$$T_0(\lambda) = \frac{E_d^{0+}(\lambda)}{E_d^{TOA}(\lambda)} \quad (7)$$

The band-integrated above-water marine reflectance is:

$$\rho_w^{0+(B)} = \pi \frac{\int \omega(\lambda)L_w^{0+}(\lambda)d\lambda}{\int \omega(\lambda)E_d^{0+}(\lambda)d\lambda} \quad (8)$$

Which gives, after substitution of Eqs. 6 and 7:

$$\rho_w^{0+(B)} = \frac{\int \omega(\lambda)T_0(\lambda)\rho_w^{0+}(\lambda)E_d^{TOA}(\lambda)d\lambda}{\int \omega(\lambda)T_0(\lambda)E_d^{TOA}(\lambda)d\lambda} \quad (9)$$

Now $\rho_w^{TOA(B)}$ can be re-written, using Eqs. 2, 6, and 7:

$$\rho_w^{TOA(B)} = \frac{\int \omega(\lambda)T_v(\lambda)T_0(\lambda)\rho_w^{0+}(\lambda)E_d^{TOA}(\lambda)d\lambda}{\int \omega(\lambda)E_d^{TOA}(\lambda)d\lambda} \quad (10)$$

For relatively narrow spectral bands such as the SEVIRI VIS06 and VIS08 bands, with spectral response shown in Fig. 1, Eq. 10 simplifies to $\rho_w^{TOA(B)} = T_v^{(B)}T_0^{(B)}\rho_w^{0+(B)}$. The atmospheric correction of VIS06, denoted by (0.6) superscript, described in Neukermans et al. (2009) solves Eq. 5 for $\rho_w^{0+(0.6)}$. For a very broad spectral band such as SEVIRI's HRV band, however, each component of the convolution in the spectral integral in Eq. 10 may show strong spectral variability as shown in Fig. 1 and this simplification may no longer be valid. To minimize uncertainties of atmospheric correction and calibration of the HRV band, the spatial variability of HRV marine reflectance within each VIS06 pixel is used as a small perturbation to the VIS06 derived marine reflectance. The approach is described in the next section.

2.2. VIS06 marine reflectance on the HRV grid

To use the higher spatial resolution information of the HRV band, first a relationship is established between the marine reflectances in the HRV and VIS06 bands taking account of the different sensor response functions and the different effective atmospheric transmittances. Then this relationship is used to estimate the spatial variability of $\rho_w^{0+(0.6)}$ on the fine HRV grid using the spatial anomaly of TOA HRV reflectance.

2.2.1. Relating marine reflectances in the HRV and VIS06 bands

Re-examining Fig. 1, it can be seen that in the case of the HRV, the effects of low atmospheric transmittances (T_0 and T_v) to the spectral integral in Eq. 10 are limited: in the spectral range 0.75–0.90 μm , the strong atmospheric absorption dominated by water vapour goes with a low $\rho_w^{0+}(\lambda)$ and important Rayleigh effects on transmittances in the range 0.35–0.45 μm coincide with a low $\omega(\lambda)$. Hence, atmospheric transmittances in the range 0.45–0.75 μm contribute most strongly to the spectral integral in Eq. 10. In this range the atmospheric transmittances are reasonably smooth and high. A good linear correlation between $\rho_w^{0+(0.6)}$ and $\rho_w^{0+(HRV)}$ is observed as shown in Fig. 2(a). Combination of the observations described above suggests that $\rho_w^{TOA(HRV)}$ can be approximated by

$$\rho_w^{TOA(HRV)} \approx (A\rho_w^{0+(0.6)} + B)T_{0,v}^{(0.6)}\alpha^{m/2} \quad (11)$$

where $T_{0,v}^{(0.6)}$ is the two-way (sun-sea and sea-sensor) atmospheric transmittance for a given two-way air mass m

$$m = \frac{1}{\cos\theta_v} + \frac{1}{\cos\theta_0} \quad (12)$$

in the VIS06 band:

$$T_{0,v}^{(0.6)} = \frac{\int \omega(\lambda)T_v(\lambda)T_0(\lambda)E_d^{TOA}(\lambda)d\lambda}{\int \omega(\lambda)E_d^{TOA}(\lambda)d\lambda} \quad (13)$$

The values of A and α in Eq. 11 have been obtained by spectral convolution of 67 measured hyperspectral seaborne spectra with: (a) the HRV and VIS06 band sensor response functions according to Eq. 8 and (b) with the sensor response functions and the appropriate

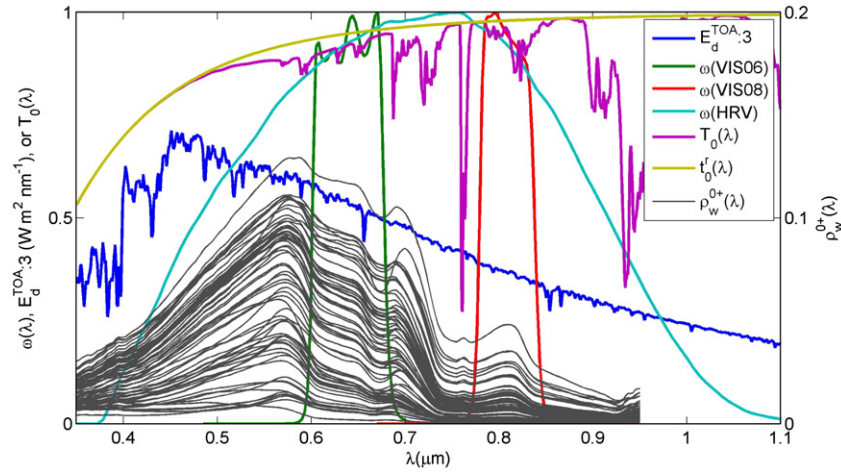


Fig. 1. Normalized spectral response, $\omega(\lambda)$ of SEVIRI's VIS06, VIS08, and HRV bands, and one-way total (T_0) and Rayleigh transmittance, t_0^r , for a vertical atmospheric path and the US standard atmosphere model obtained from LOWTRAN simulations. Thin lines represent above-water marine reflectance spectra, $\rho_w^{0+}(\lambda)$, recorded with hyperspectral above-water TriOS Ramses radiometers in the southern North Sea between 2001 and 2010. The reader is referred to Ruddick et al. (2006) for details on the seaborne measurement protocol. Spectrum of solar irradiance at TOA from Thuillier et al. (2003).

atmospheric transmittances according to Eqs. 10 and 13. The atmospheric transmittances are obtained from LOWTRAN simulations for $m=2$ and the US standard atmosphere model, shown in Fig. 1. These include Rayleigh transmittances, aerosol transmittances, and gas transmittances for ozone, carbon dioxide, and water vapour. The results of these calculations are shown in Fig. 2 and give (a) $A=0.71(\pm 0.01)$ and (b) $A\alpha=0.68(\pm 0.01)$ and hence $\alpha=0.96(\pm 0.02)$.

2.2.2. Estimating spatial variability of $\rho_w^{0+(0.6)}$ from HRV spatial anomaly

Each pixel in the VIS06 grid corresponds to 3×3 pixels in the HRV grid. The spatial variability of $\rho_w^{TOA(HRV)}$ within each VIS06 pixel is used to represent a small perturbation to the marine reflectance retrieved from the VIS06 band. Let the bar superscript denote the mean value of 9 HRV pixels corresponding to one pixel in the VIS06 grid. The spatial anomaly of the HRV signal within the VIS06 grid is:

$$\hat{\rho}_{tot}^{TOA(HRV)} = \rho_{tot}^{TOA(HRV)} - \bar{\rho}_{tot}^{TOA(HRV)} \quad (14)$$

The spatial average of Eq. 5 is given by:

$$\bar{\rho}_{tot}^{TOA(HRV)} = \bar{\rho}_r^{TOA(HRV)} + \bar{\rho}_a^{TOA(HRV)} + \bar{\rho}_w^{TOA(HRV)} \quad (15)$$

Subtraction of Eq. 15 from Eq. 5 gives the spatial anomaly of $\rho_{tot}^{TOA(HRV)}$ within the VIS06 grid pixels as:

$$\hat{\rho}_{tot}^{TOA(HRV)} = \hat{\rho}_a^{TOA(HRV)} + \hat{\rho}_r^{TOA(HRV)} + \hat{\rho}_w^{TOA(HRV)} \quad (16)$$

It is assumed that the Rayleigh and aerosol reflectances are spatially constant within each $3 \text{ km} \times 6 \text{ km}$ VIS06 pixel:

$$\hat{\rho}_a^{TOA(HRV)} = 0 \text{ and } \hat{\rho}_r^{TOA(HRV)} = 0 \quad (17)$$

Eq. 16 then simplifies to:

$$\hat{\rho}_{tot}^{TOA(HRV)} = \hat{\rho}_w^{TOA(HRV)} \quad (18)$$

Now, let $\rho_w^{0+(0.6)}$ and $T_{0,v,\otimes}^{(0.6)}$ denote the above-water marine reflectance and the two-way total transmittance in the VIS06 band on the HRV grid, respectively and m_\otimes denote the air mass on the HRV grid. From Eq. 11 and subject to the underlying approximation we have:

$$\rho_w^{TOA(HRV)} = (A\rho_w^{0+(0.6)} + B)T_{0,v,\otimes}^{(0.6)}\alpha^{m_\otimes/2} \quad (19)$$

and

$$\bar{\rho}_w^{TOA(HRV)} = (A\bar{\rho}_w^{0+(0.6)} + B)\bar{T}_{0,v,\otimes}^{(0.6)}\alpha^{m_\otimes/2} \quad (20)$$

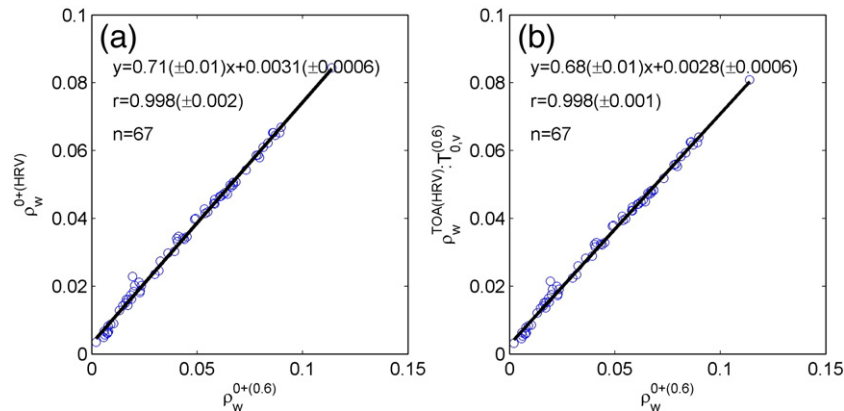


Fig. 2. (a) Linear regression of above-water marine reflectance in the HRV and the VIS06 bands and (b) linear regression of marine reflectance of the HRV band at TOA, normalized by two-way atmospheric transmittance in the VIS06 band vs. above-water marine reflectance in the VIS06 band.

where $\bar{\rho}_{w,\otimes}^{0+(0.6)} = \rho_w^{0+(0.6)}$, $\bar{T}_{0,v,\otimes}^{(0.6)} = T_{0,v}^{(0.6)}$, and $\bar{m}_\otimes = m$. Within each VIS06 grid pixel it is reasonable to assume that $T_{0,v,\otimes}^{(0.6)} \approx T_{0,v}^{(0.6)}$ and $m_\otimes \approx m$. Substitution of Eqs. 19 and 20 in Eq. 18 then gives:

$$\hat{\rho}_{tot}^{TOA(HRV)} = A(\rho_{w,\otimes}^{0+(0.6)} - \rho_w^{0+(0.6)})T_{0,v}^{(0.6)}\alpha^{m/2} \quad (21)$$

and so

$$\rho_{w,\otimes}^{0+(0.6)} = \rho_w^{0+(0.6)} + \frac{\hat{\rho}_{tot}^{TOA(HRV)}}{AT_{0,v}^{(0.6)}\alpha^{m/2}} \quad (22)$$

The first term in Eq. 22 is known for each VIS06 grid pixel. The second term represents the spatial variation of $\rho_w^{0+(0.6)}$ on the HRV grid within each VIS06 grid pixel. It is computed from the spatial anomaly of the HRV total reflectance at TOA (= spatial anomaly of HRV marine reflectance at TOA) after modification to account for differences in atmospheric transmittances and spectral convolution with marine reflectances between the VIS06 and HRV bands. An uncertainty estimate on $\rho_{w,\otimes}^{0+(0.6)}$ is derived in Section 2.4.2.

2.3. Improvements of the atmospheric correction of the SEVIRI VIS06 and VIS08 bands

The atmospheric correction of the VIS06 and VIS08 bands described by Neukermans et al. (2009) solves Eq. 5 for the VIS06 and VIS08 bands simultaneously using two assumptions:

1. The VIS06:VIS08 band ratio of marine reflectances is constant in space and time:

$$\sigma = \frac{\rho_w^{0+(0.6)}}{\rho_w^{0+(0.8)}} \quad (23)$$

For this study, σ was recalibrated to account for the small difference in spectral response of the SEVIRI radiometer on board MSG-2 as compared to MSG-1. Ordinary least-squares regression through the origin of $\rho_w^{0+(0.6)}$ vs. $\rho_w^{0+(0.8)}$ from in situ hyperspectral measurements of $\rho_w^{0+}(\lambda)$ as described by Neukermans et al. (2009) gives $\sigma = 6.09 \pm 0.16$. This is not significantly different from the value of $\sigma = 6.07 \pm 0.30$ used for MSG-1 by Neukermans et al. (2009).

2. The VIS06:VIS08 band ratio of aerosol reflectances at TOA is spatially homogeneous over the SEVIRI scene:

$$\varepsilon = \frac{\rho_a^{TOA(0.6)}}{\rho_a^{TOA(0.8)}} \quad (24)$$

So that $\rho_w^{0+(0.6)}$ can be expressed as (see Eq. 20 in Neukermans et al., 2009):

$$\rho_w^{0+(0.6)} = \sigma \frac{\rho_c^{(0.6)} - \varepsilon \rho_c^{(0.8)}}{t_{0,v}^{a(0.8)}(\gamma\sigma - \varepsilon)} \quad (25)$$

Where $\rho_c^{(B)}$ denotes the Rayleigh and gas corrected reflectance in band B:

$$\rho_c^{(B)} = \frac{\rho_{tot}^{TOA(B)} - \rho_r^{TOA(B)}}{t_{0,v}^{r,g(B)}} \quad (26)$$

and γ is the VIS06:VIS08 band ratio of two-way aerosol transmittances, which is close to 1.

An estimate of ε (Eq. (24)) is obtained on an image-by-image basis from the VIS06:VIS08 band ratio of $\rho_c^{(B)}$ over clear waters pixels so that $\rho_c^{(B)}$ is dominated by the aerosol signal with negligible contribution from the water (Neukermans et al., 2009). The two year SEVIRI archive was first processed (atmospheric correction, followed by application of the [SPM] algorithm in Eq. 21 in Neukermans et al., 2009) using the clear water pixels areas described in Neukermans et al. (2009) and shown as black rectangles in Fig. 3. In the present study, clear water pixels are redefined as those pixels having [SPM] below 3 mg L^{-1} (corresponding to $\rho_w^{0+(0.6)} < 0.01$ and $\rho_w^{0+(0.8)} < 0.002$) for 95% of the observations from the 2-year SEVIRI dataset and are outlined by the red polygons in Fig. 3. The newly defined clear water areas exclude the turbid water plume that can be seen in Fig. 3 and are distributed more evenly throughout the study area.

Neukermans et al. (2009) estimate ε and its uncertainty, $\Delta\varepsilon$, from the mean and standard deviation of $\rho_c^{(0.6)}:\rho_c^{(0.8)}$ for these pixels, assuming that the ratios are normally distributed. An example is shown in Fig. 4(a). This assessment of ε is, however, sensitive to data outliers and noise, and requires the band ratios to be approximately normally distributed. Especially the noise of the reflectance ratios may be large for SEVIRI due to digitization effects (see also Section 2.4.1). Alternatively, ε can be assessed from the slope of the $\rho_c^{(0.6)}$ vs. $\rho_c^{(0.8)}$ regression as shown in Fig. 4(b). An iteratively reweighted least squares technique using the MATLAB robustfit.m routine is applied, where $\Delta\varepsilon$ is estimated from the standard error of the slope estimate. This approach minimizes effects of outliers and data noise and is independent of the normality of the reflectance ratio distribution. Moreover, the offset of the regression line reflects small uncertainties in the calibration of the SEVIRI sensor and the Rayleigh and gas corrections, and allows to correct for these uncertainties through subtraction of the offset from $\rho_c^{(0.6)}$. Typical values of this offset are between -0.0051 and 0.0126 (5 and 95th percentiles) with a median of 0.0028 for 15,384 observations. This procedure is effectively a vicarious calibration of SEVIRI performed on an image-by-image basis without the need to assume a temporally constant aerosol type. We further note that if the clear water areas include pixels with $[\text{SPM}] > 3 \text{ mg L}^{-1}$, which occurs in 5% of the observations in 2008–2009 by definition, the robust regression routine is expected to strongly reduce their effect on the estimation of ε .

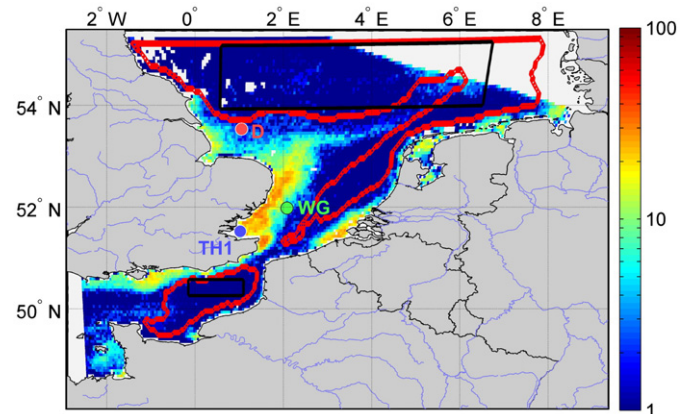


Fig. 3. Identification of clear water pixels from which the ratio of aerosol reflectance ε is obtained. The black rectangles delineate the clear water pixels identified by Neukermans et al. (2009), while the red polygons delineate the clear water pixels used in this study. Background: [SPM] (in mg L^{-1}) map from SEVIRI on February 11, 2008 at 10:45 UTC. The location of the Cefas SmartBuoys at Warp Anchorage (TH1), West Gabbard (WG), and Dowsing (D) is also indicated.

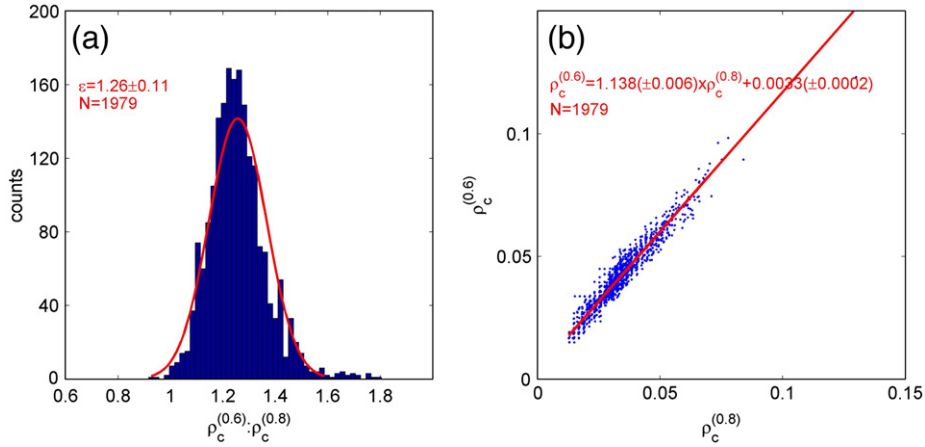


Fig. 4. Example of the estimation of the VIS06:VIS08 ratio of aerosol reflectances, ε , on April 9, 2008 at 09:45 UTC from the Rayleigh and gas corrected reflectances, ρ_c , in the VIS06 and VIS08 bands of clear water pixels via (a) the mean and standard error of $\rho_c^{(0.6)}$: $\rho_c^{(0.8)}$ values, shown as the normal fit to the histogram, or (b) via linear regression of $\rho_c^{(0.6)}$ vs. $\rho_c^{(0.8)}$, where uncertainties on regression coefficients are given by their standard error. N is the number of pixels.

2.4. Uncertainty estimation on marine reflectance

The uncertainty on $\rho_w^{0+(0.6)}$ associated with the assumptions of the atmospheric correction in Eqs. 23 and 24 is given by Neukermans et al. (2009):

$$\Delta\rho_w^{0+(0.6)} = \frac{1}{t_{0,v}^{a(0.8)}(\gamma\sigma - \varepsilon)} \left[\left(\rho_a^{TOA(0.8)} \sigma \Delta\varepsilon \right)^2 + \left(\rho_w^{0+(0.8)} \varepsilon t_{0,v}^{a(0.8)} \Delta\sigma \right)^2 \right]^{1/2} \quad (27)$$

The first component ($\Delta_a \rho_w^{0+(0.6)}$), is related to the aerosol turbidity, while the second component ($\Delta_w \rho_w^{0+(0.6)}$) is related to the water turbidity. The contribution of each component can be understood by simplifying with $t_{0,v}^{a(0.8)} = 1 = \gamma$ and taking a typical value of $\varepsilon = 1.02 \pm 0.01$. Then $\Delta_a \rho_w^{0+(0.6)} = 0.012 \rho_a^{TOA(0.8)}$ and $\Delta_w \rho_w^{0+(0.6)} = 0.032 \rho_w^{0+(0.8)}$.

In what follows, we extend this uncertainty estimate to include uncertainties associated with digitization effects at TOA in the VIS06 and VIS08 bands.

2.4.1. Digitization uncertainties

Total reflectance at TOA for VIS06 and VIS08 bands is obtained through calibration of the SEVIRI level 1.5 data. Count data (K) are transformed into total radiance at TOA, L_{tot}^{TOA} (units: $\text{W m}^{-2} \text{sr}^{-1} \mu\text{m}^{-1}$), by applying the appropriate calibration coefficients (c_f) and offset values (r_0) (see Table 2):

$$L_{tot}^{TOA(B)} = \frac{10(c_f^{(B)}K + r_0^{(B)})}{(\lambda_0^{(B)})^2} \quad (28)$$

where $\lambda_0^{(B)}$ is band B's central wavelength. $L_{tot}^{TOA(B)}$ is then converted to total reflectance at TOA:

$$\rho_{tot}^{TOA(B)} = \frac{\pi d^2 L_{tot}^{TOA(B)}}{A_0^{(B)} E_0^{TOA(B)} \cos\theta_0} \quad (29)$$

Table 2

Central wavelengths, $\lambda_0^{(B)}$, extraterrestrial solar irradiance, $E_0^{TOA(B)}$, and calibration correction factors, $A_0^{(B)}$ (Ham & Sohn, 2010; Sohn, unpublished results) for the SEVIRI MSG2 VIS06 and VIS08 bands.

Band	$\lambda_0^{(B)}$ (μm)	$c_f^{(B)}$ ($\text{mW m}^{-2} \text{sr}^{-1} (\text{cm}^{-1})^{-1}$)	$r_0^{(B)}$ ($\text{mW m}^{-2} \text{sr}^{-1} (\text{cm}^{-1})^{-1}$)	$E_0^{TOA(B)}$ ($\text{W m}^{-2} \mu\text{m}^{-1}$)	$A_0^{(B)}$
VIS06	0.635	0.020135, 0.020419 ^a	-1.026910, -1.041374 ^a	1618.0	0.92
VIS08	0.810	0.025922, 0.026168 ^a	-1.32202, -1.334553 ^a	1113.0	0.94

^a December 9, 2008, 12:00 UTC–September 13, 2009, 18:00 UTC.

where d is the Sun–Earth distance in astronomical units (AU), θ_0 is the sun zenith angle calculated from position, date and time, $E_0^{TOA(B)}$ is the extraterrestrial solar irradiance at TOA for band B at 1 AU (in $\text{W m}^{-2} \mu\text{m}^{-1}$). Calibration correction factors, $A_0^{(B)}$, for the MSG-2 SEVIRI VIS06 and VIS08 channels of 0.92 and 0.94 are given by Ham and Sohn (2010) and Sohn (unpublished results), respectively, and are given in Table 2.

The uncertainty on the TOA reflectance due to digitization can be derived from Eqs. 28 and 29:

$$\Delta\rho_{tot}^{TOA(B)} = \frac{10c_f^{(B)}\pi d^2}{(\lambda_0^{(B)})^2 E_0^{TOA(B)} A_0^{(B)} \cos\theta_0} \quad (30)$$

Digitization uncertainty increases with increasing sun zenith angle, $0^\circ \leq \theta_0 \leq 80^\circ$, between 0.001 and 0.006 for the VIS06 band and between 0.001 and 0.007 for the VIS08 band, as shown in Table 3. The uncertainty on $\rho_w^{0+(0.6)}$ due to digitization in VIS06 and VIS08 at TOA, $\Delta_d \rho_w^{0+(0.6)}$, is obtained using the formula for first order error propagation (ISO, 1995):

$$\Delta_d \rho_w^{0+(0.6)} = \left[\left(\frac{\partial \rho_w^{0+(0.6)}}{\partial \rho_{tot}^{TOA(0.6)}} \Delta \rho_{tot}^{TOA(0.6)} \right)^2 + \left(\frac{\partial \rho_w^{0+(0.6)}}{\partial \rho_{tot}^{TOA(0.8)}} \Delta \rho_{tot}^{TOA(0.8)} \right)^2 \right]^{1/2} \quad (31)$$

Partial derivation of Eq. 25 to $\rho_{tot}^{TOA(0.6)}$ and $\rho_{tot}^{TOA(0.8)}$ using Eq. 26 gives:

$$\Delta_d \rho_w^{0+(0.6)} = \frac{\sigma}{t_{0,v}^{a(0.8)}(\gamma\sigma - \varepsilon)} \left[\left(\frac{\Delta \rho_{tot}^{(0.6)}}{t_{0,v}^{r,g(0.6)}} \right)^2 + \left(\frac{\varepsilon \Delta \rho_{tot}^{(0.8)}}{t_{0,v}^{r,g(0.8)}} \right)^2 \right]^{1/2} \quad (32)$$

This digitization uncertainty is evaluated in Table 3 for a typical $\theta_v = 60^\circ$ (corresponding to the middle of the SEVIRI North Sea scene in Fig. 3), $\varepsilon = 1.02 \pm 0.01$, $\gamma = 1$, typical gas concentrations

Table 3
Contribution of each component in Eq. 33 to $\Delta\rho_w^{0+(0.6)}$ for varying sun zenith angles (θ_0), clear (CA, $\tau_a(550 \text{ nm}) = 0.01$) and turbid (TA, $\tau_a(550 \text{ nm}) = 0.5$) atmospheres, and clear (CW, $\rho_w^{0+(0.6)} = 0.004$) and turbid (TW, $\rho_w^{0+(0.6)} = 0.07$) waters. Viewing geometry values typical for the SEVIRI North Sea area were taken: $\theta_v = 60^\circ$ and $\Delta\varphi = 40^\circ$, typical gas concentrations and $\varepsilon = 1.02 \pm 0.01$, $\gamma = 1$, and $\sigma = 6.09 \pm 0.16$. Air mass and digitization uncertainty for total TOA reflectance in the VIS06 ($\Delta\rho_{\text{tot}}^{\text{TOA}(0.6)}$) and VIS08 bands ($\Delta\rho_{\text{tot}}^{\text{TOA}(0.8)}$) computed using Eq. 30 are also shown.

θ_0	m	$\Delta\rho_{\text{tot}}^{\text{TOA}(0.6)}$	$\Delta\rho_{\text{tot}}^{\text{TOA}(0.8)}$	$\Delta_d\rho_w^{0+(0.6)}$		$\Delta_a\rho_w^{0+(0.6)}$		$\Delta_w\rho_w^{0+(0.6)}$		$\Delta\rho_w^{0+(0.6)}$	
				CA	TA	CA	TA	CW	TW	CA, CW	TA, TW
0	3.00	0.0011	0.0012	0.002300	0.002841	0.000006	0.000562	0.000021	0.000370	0.002300	0.002920
10	3.02	0.0011	0.0012	0.002337	0.002889	0.000007	0.000558	0.000021	0.000370	0.002337	0.002965
20	3.06	0.0011	0.0013	0.002455	0.003055	0.000008	0.000645	0.000021	0.000370	0.002455	0.003144
30	3.15	0.0012	0.0014	0.002674	0.003352	0.000010	0.000775	0.000021	0.000370	0.002674	0.003460
40	3.31	0.0014	0.0015	0.003043	0.003858	0.000013	0.000973	0.000021	0.000370	0.003043	0.003996
50	3.56	0.0016	0.0018	0.003667	0.004734	0.000017	0.001245	0.000021	0.000370	0.003667	0.004909
60	4.00	0.0021	0.0024	0.004804	0.006393	0.000022	0.001600	0.000021	0.000370	0.004804	0.006601
70	4.92	0.0031	0.0035	0.007311	0.010986	0.000033	0.002672	0.000021	0.000370	0.007311	0.011312
80	7.76	0.0061	0.0068	0.016202	0.031027	0.000053	0.004607	0.000021	0.000370	0.016202	0.031369

(320 Dobson units for ozone and 29.3 kg m^{-2} for precipitable water content) and for clear (CA) and turbid (TA) atmospheres with aerosol optical thicknesses, $\tau_a(550 \text{ nm})$, of 0.01 and 0.5, respectively. In the clearest waters where $\rho_w^{0+(0.6)}$ is about 0.002–0.006 and for moderate air mass, the magnitude of the digitization uncertainty is comparable to $\rho_w^{0+(0.6)}$. Digitization uncertainty increases rapidly for air masses above 4, reaching 0.03 for turbid atmospheres and an air mass of 7.8.

The uncertainty due to digitization is added to the uncertainty associated with the atmospheric correction to give:

$$\Delta\rho_w^{0+(0.6)} = \left[\left(\Delta_d\rho_w^{0+(0.6)} \right)^2 + \left(\Delta_a\rho_w^{0+(0.6)} \right)^2 + \left(\Delta_w\rho_w^{0+(0.6)} \right)^2 \right]^{1/2} \quad (33)$$

The contribution of each component in Eq. 33 to $\Delta\rho_w^{0+(0.6)}$ is further evaluated in Table 3 for a relative azimuth angle of 40° and for clear (CW) and turbid water (TW) with $\rho_w^{0+(0.6)}$ of 0.004 and 0.07, respectively. Even for turbid water and a turbid atmosphere the digitization uncertainty is the dominant contributor to the total uncertainty on marine reflectance.

2.4.2. Uncertainty estimate of marine reflectance in the VIS06 band on the HRV grid

Using the formula for first order error propagation (ISO, 1995), the uncertainty on $\rho_{w,\otimes}^{0+(0.6)}$ introduced by uncertainties in $\rho_w^{0+(0.6)}$, A , and α can be estimated from an expression analogous to Eq. 31. Partial derivation of the expression in Eq. 22 to each parameter then gives:

$$\Delta\rho_{w,\otimes}^{0+(0.6)} = \left[\left(\Delta\rho_w^{0+(0.6)} \right)^2 + \left(\frac{\rho_{\text{tot}}^{\text{TOA}(\text{HRV})}}{AT_{\text{tot}}^{(0.6)} \alpha^{m/2}} \right)^2 \left(\left(\frac{\Delta A}{A} \right)^2 + \left(\frac{m\Delta\alpha}{2\alpha} \right)^2 \right) \right]^{1/2} \quad (34)$$

With $A = 0.71$, $\Delta A = 0.01$, $\alpha = 0.96$, $\Delta\alpha = 0.02$, and $\Delta\rho_w^{0+(0.6)}$ from Eq. 33.

2.5. Retrieval and uncertainty estimate of turbidity

The semi-empirical single band turbidity retrieval algorithm of Nechad et al. (2009) for the SEVIRI VIS06 band was calibrated using in situ data of marine reflectance and turbidity, T . Non-linear regression was applied on 68 simultaneous observations of T and marine reflectance in the southern North Sea obtained in 2007–2010 (see Nechad et al., 2010 for details on curve fitting and Neukermans, 2012 for data selection criteria). T , expressed in Formazine Nephelometric Units (FNU), was recorded on 10 mL subsamples with a Hach 2100P portable turbidity instrument. This instrument measures the ratio of light scattered at an angle of 90° at a wavelength of 860 nm

to forward transmitted light, as compared to the same ratio for a standard suspension of Formazine, in accordance with ISO, 7027 (1999). Six replicate measurements were mean-averaged to obtain T . Marine reflectance in the VIS06 band was obtained after Eq. 8 from hyperspectral above-water measurements of $L_w^+(\lambda)$ and $E_d^+(\lambda)$ with TriOS RAMSES radiometers.

Calibration of the algorithm (Nechad et al., 2009)

$$T = \frac{A_T \rho_w^{0+(0.6)}}{C - \rho_w^{0+(0.6)}} + B_T \quad (35)$$

gives $A_T = 35.8 \pm 3.8$ FNU and $B_T = -0.1 \pm 0.9$ FNU. The value of C is band specific, giving $C = 0.1639$ for the SEVIRI VIS06 band. The algorithm in Eq. 35 is applied without the offset B_T and is shown in Fig. 5.

The uncertainty on remotely sensed T , resulting from the combined uncertainties on marine reflectance and the parameter A_T is (Neukermans et al., 2009):

$$\Delta T = \frac{1}{C - \rho_w^{0+(0.6)}} \left[\left(\rho_w^{0+(0.6)} \Delta A_T \right)^2 + \left(\frac{A_T C \Delta \rho_w^{0+(0.6)}}{C - \rho_w^{0+(0.6)}} \right)^2 \right]^{1/2} \quad (36)$$

Replacing $\rho_w^{0+(0.6)}$ by $\rho_{w,\otimes}^{0+(0.6)}$ and $\Delta\rho_w^{0+(0.6)}$ by $\Delta\rho_{w,\otimes}^{0+(0.6)}$ gives T and ΔT on the HRV grid, denoted by T_\otimes and ΔT_\otimes .

2.6. Retrieval and uncertainty estimate of PAR attenuation

Many studies have illustrated that the variability in light attenuation is primarily driven by [SPM] in turbid coastal waters (Devlin et al., 2008; Xu et al., 2005) and in lagoons and estuaries (Christian & Sheng, 2003; Lawson et al., 2007; Painting et al., 2007). From a spatially extensive survey of vertical profiles of PAR and [SPM] in coastal and offshore UK waters a strong linear relationship ($R^2 = 0.98$) between the water column mean [SPM], S , and the water column mean attenuation coefficient of PAR, K_{PAR} , was found (Devlin et al., 2008):

$$K_{\text{PAR}} = 0.325(\pm 0.06) + 0.066(\pm 0.002) \times S \quad (37)$$

where S varied between 0.1 mg L^{-1} and 250 mg L^{-1} , with most values below 50 mg L^{-1} and K_{PAR} varied between 0.3 m^{-1} and 15 m^{-1} with most values below 3 m^{-1} . This model has been shown to work well in turbid waters, dominated by suspended sediments (Devlin et al., 2008). A SEVIRI K_{PAR} product is derived from a combination of Eq. 37 and the single band [SPM] retrieval algorithm of Nechad et al. (2010), calibrated for the SEVIRI VIS06 band:

$$S = \frac{A_S \rho_w^{0+(0.6)}}{C - \rho_w^{0+(0.6)}} + B_S \quad (38)$$

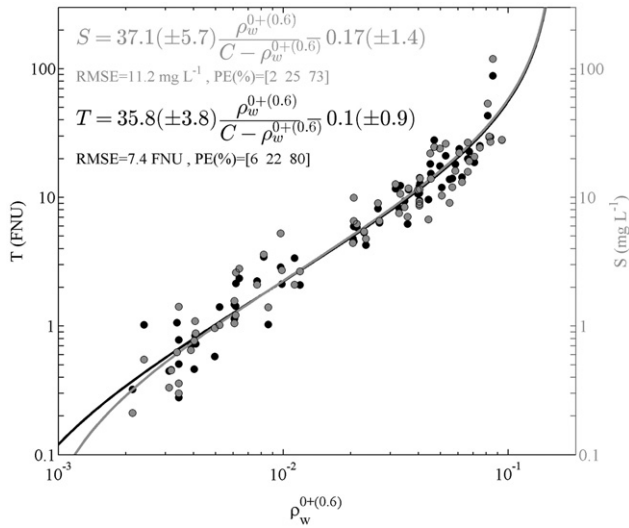


Fig. 5. Scatter plot of 68 seaborne measurements of marine reflectance in the VIS06 band, and turbidity (T) and [SPM] (S). The RMSE and the 5–50–95th percentiles of the prediction error (PE = ratio of the absolute value of the difference between the model prediction from the measured value to the measured value) of each fit are also given. The black and grey lines represent the SEVIRI VIS06 retrieval algorithms for T and S from Nechad et al. (2009) and Nechad et al. (2010), respectively.

with calibration factors $A_S = 37.1 \pm 5.7 \text{ g m}^{-3}$ and $B_S = -0.17 \pm 1.4 \text{ g m}^{-3}$, obtained from the same in situ dataset as for the calibration of the T algorithm. The [SPM] algorithm, shown in Fig. 5, is also applied without the offset. Eq. 36 gives an expression for the uncertainty on S when A_T is replaced with A_S . The uncertainty on the SEVIRI K_{PAR} product, introduced by uncertainties on S and the slope and offset of the model in Eq. 37 is:

$$\Delta K_{PAR} = \left[(0.066\Delta S)^2 + (0.002S)^2 + 0.06^2 \right]^{1/2} \quad (39)$$

Replacing $\rho_w^{0+(0.6)}$ by $\rho_{w,\otimes}^{0+(0.6)}$ and $\Delta\rho_w^{0+(0.6)}$ by $\Delta\rho_{w,\otimes}^{0+(0.6)}$ in Eq. 38 gives K_{PAR} and ΔK_{PAR} on the HRV grid, denoted by $K_{PAR,\otimes}$ and $\Delta K_{PAR,\otimes}$.

2.7. Validation of SEVIRI turbidity and PAR attenuation products

2.7.1. SmartBuoy measurements of turbidity and PAR attenuation

Half-hourly measurements of physical, chemical, optical, and biological variables are made in UK shelf seas from moored platforms (SmartBuoys; Mills et al., 2003), operated by the Centre for Environment, Fisheries and Aquaculture Sciences (Cefas) on a regular basis since 2001. Several SmartBuoys were operational in the southern North sea in 2008–2009: Warp Anchorage (TH1) (51.5235°N, 1.0240°E) and West Gabbard (WG) (51.9802°N, 2.0828°E), and since 2009 also Dowsing (D) (53.5313°N, 1.0532°E). Their location is shown in Fig. 3. Cefas SmartBuoys measure water turbidity, denoted T^{SB} , using a Seapoint turbidity meter, which records light scattered by suspended particles between 15° to 150° from a light source emitted at 880 nm. Turbidity is measured 1–2 m below the surface and expressed in Formazine Turbidity Units (FTU). PAR is recorded using three LI-COR (LI-192SB) underwater quantum sensors installed just above the surface and at 1 m and 2 m depths (units: $\mu\text{E m}^{-2} \text{ s}^{-1}$). SmartBuoy turbidity and PAR measurements are recorded during 10 minute bursts, every half hour. Every burst gives 600 scans, which were mean-averaged.

The vertical light attenuation coefficient can be derived from PAR measurements at 1 m and 2 m depth using the Lambert–Beer equation:

$$K_{PAR}^{SB} = \ln\left(\frac{\text{PAR}(1\text{m})}{\text{PAR}(2\text{m})}\right) \quad (40)$$

with uncertainty:

$$\Delta K_{PAR}^{SB} = \left[\left(\frac{\Delta\text{PAR}(1\text{m})}{\text{PAR}(1\text{m})}\right)^2 + \left(\frac{\Delta\text{PAR}(2\text{m})}{\text{PAR}(2\text{m})}\right)^2 - 2\frac{\Delta\text{PAR}(1\text{m})\Delta\text{PAR}(2\text{m})}{\text{PAR}(1\text{m})\text{PAR}(2\text{m})} \right]^{1/2} \quad (41)$$

where Δ represents the standard deviation of PAR during each burst and the third term is present because PAR(1 m) and PAR(2 m) are highly correlated with correlation coefficients above 0.95 for each SmartBuoy (simplified in Eq. 40 with $r = 1$). The above water PAR measurements, PAR(0 m), were used for data quality control based on following criterion:

$$\ln\left(\frac{\text{PAR}(0\text{m})}{\text{PAR}(1\text{m})}\right) - \ln\left(\frac{\text{PAR}(1\text{m})}{\text{PAR}(2\text{m})}\right) \leq 0.5 \ln\left(\frac{\text{PAR}(0\text{m})}{\text{PAR}(1\text{m})}\right) \quad (42)$$

This means that observations where PAR attenuation between 1 m and 2 m depth differs more than 50% from the PAR attenuation between the surface and 1 m depth are rejected. The 0.5 threshold value corresponds to the 75th percentile so that 25% of the PAR data were rejected. Unfortunately no surface PAR measurements are available at WG, so the validation of SEVIRI K_{PAR} is limited to TH1 and D.

2.7.2. Comparison of instantaneous SEVIRI-SmartBuoy observations

Cloud free SEVIRI T and K_{PAR} products, P , were regressed against corresponding SmartBuoy data, P^{SB} . Single pixel match-ups were considered, with differences in sampling time smaller than 10 min were taken. Correlation analysis and ‘least squares cubic’ regressions (York 1966), which take into account measurement uncertainties in the data, are used. The least squares cubic regression is applied after removal of outliers, identified by the MATLAB robustfit.m routine. Correlation coefficients are given with their 95% confidence intervals, obtained from bootstrapping. Details of these statistical procedures are described in the Web appendix of Neukermans et al. (2012).

Several statistics are used to quantify agreement between SEVIRI and SmartBuoys products. The Root-Mean-Square-Error (RMSE), computed after removal of outliers:

$$\text{RMSE} = \sqrt{\frac{1}{n-2} \sum_{k=1}^n (P^{SB} - P)^2} \quad (43)$$

and the 5th, 50th, and 95th percentiles of the relative absolute prediction error, PE (computed from all observations):

$$PE = \frac{|P - P^{SB}|}{P^{SB}} \quad (44)$$

and the relative bias:

$$\text{bias} = \frac{P - P^{SB}}{P^{SB}} \quad (45)$$

2.7.3. Validation of SEVIRI product time series

Continuous and cloud free SEVIRI T and K_{PAR} time series longer than 4.5 h were compared against corresponding SmartBuoy time series. SmartBuoy time series were interpolated on the SEVIRI time grid. A moving average filter with a span of 5 observations was applied twice to the SEVIRI and Cefas time series and local maxima were

identified using the findextrema.m MATLAB script of Deng (2009). In the case of multiple local maxima for SEVIRI time series, only the global maximum was retained. The timing of the global maximum of the SEVIRI product, $t(P_{\max})$, was then compared against the timing of the nearest maximum of the corresponding SmartBuoy product, $t(P_{\max}^{SB})$. Smoothed time series where the diurnal variability of P detected by SEVIRI ($P_{\max} - P_{\min}$) was smaller than the daily mean standard error on P were not considered. Also, time series where the diurnal variability detected by the SmartBuoy was smaller than a certain fraction of the maximum SmartBuoy data for a given day were not considered. This fraction was arbitrarily set to 0.4 for T and 0.2 for K_{PAR} . The agreement in timing of the maximum between SEVIRI and SmartBuoy time series of a product P is quantified by the mean and standard deviation and the 5th, 50th, and 95th percentiles of the timing bias, $bias_t = t(P_{\max}) - t(P_{\max}^{SB})$, and the timing prediction error, $PE_t = |t(P_{\max}) - t(P_{\max}^{SB})|$.

3. Results

3.1. HRV imagery

An example of the improvement in spatial resolution achieved by the use of the HRV band is shown in Fig. 6 for turbidity on February 11, 2008 at 13:00 UTC.

3.2. Comparison of instantaneous SEVIRI-SmartBuoy observations

3.2.1. Turbidity observations

A total of 3068 SEVIRI-SmartBuoy T match-ups were observed at TH1, WG, and D. Scatter plots of T vs. T^{SB} are shown in Fig. 7(a). Observations with over 100% uncertainty on $\rho_w^{0+(0.6)}$ (obtained from Eq. 37, see grey dots in Fig. 7(a) were removed, giving 2598 ($=n_v$) remaining observations. Least squares cubic regression was applied to this dataset after removal of 51 ($=n_x$) outliers. Equation and statistics of the regression are shown in Table 4. A good correlation is observed between T and T^{SB} with correlation coefficient $r = 0.933 \pm 0.006$. On average, T is underestimated by SEVIRI by 14%, with a median prediction error of 29% and an RMSE of 5.8 FNU. In 80% of the cases T is within 53% of T^{SB} and in 95% of the cases within 80% (see Table 4). For validation of the high spatial resolution T product, T_{∞} , observations neighbouring cloud or low aerosol transmittance (where $t_{0,v}^{a(0.6)} < 0.85$) pixels were further removed (shown by grey dots in Fig. 7(b)), giving 1412 remaining match-ups. The correlation coefficient, regression equation, and RMSE found for T_{∞} vs. T^{SB} were similar to the values found for the low spatial resolution T vs. T^{SB}

comparison. However, the scatter in the T_{∞} vs. T^{SB} plots is higher with higher spread in the 5–95th percentiles of PE and bias and higher median underestimation by SEVIRI of 20% (see Table 4).

3.2.2. PAR attenuation observations

A total of 1492 SEVIRI-SmartBuoy K_{PAR} match-ups were observed at TH1 and D. Scatter plots of K_{PAR} vs. K_{PAR}^{SB} are shown in Fig. 7(c). Observations with over 100% uncertainty on $\rho_w^{0+(0.6)}$ or quality flagged PAR data (see Eq. (42)) are shown as grey dots in Fig. 7(c). These observations were removed from the dataset, giving 988 remaining match-ups. Equation and statistics of the regression are shown in Table 4. A good correlation is observed between K_{PAR} and K_{PAR}^{SB} with correlation coefficient $r = 0.926 \pm 0.008$. Overall, SEVIRI overestimates K_{PAR} by 9% on average, with a median prediction error of 18% and an RMSE of 0.34 m^{-1} . In 80% of the cases K_{PAR} is within 39% of K_{PAR}^{SB} and in 95% of the cases within 81% (see Table 4). Analogously to the validation of T_{∞} , observations neighbouring cloud or low aerosol transmittance pixels were further removed (shown by grey dots in Fig. 7(d)), giving 424 remaining match-ups for $K_{PAR,\infty}$. The correlation coefficient, regression line, and prediction errors of $K_{PAR,\infty}$ vs. K_{PAR}^{SB} are comparable to the values found for the low spatial resolution product. The overestimation of K_{PAR} by SEVIRI for the high resolution product decreased by 4% on average compared to the low resolution product.

3.3. Validation of SEVIRI product time series

3.3.1. Time series of turbidity

A total of 105 continuous and cloud free SEVIRI/SmartBuoy T time series longer than 4.5 h were found of which 49 satisfied the selection criteria described in Section 2.7.3. A random selection of 12 time series of T derived from SEVIRI and the SmartBuoy are shown in Figs. 8 and 9. The in situ data shows strong variability with a period of about 6 h, typical of resuspension dynamics induced by a semi-diurnal tide, but strong wind and wave action also affect advection and resuspension of sediments from the bottom. Overall, the diurnal variability of T detected by the SmartBuoy is picked up well by SEVIRI, albeit with some exceptions (e.g. Fig. 9h,j). In general, the high spatial resolution time series of SEVIRI are noisier than the low resolution time series. For comparison, data availability from MODIS Aqua, MODIS Terra, and MERIS ENVISAT is also indicated in Figs. 8 and 9, clearly showing the tremendous increase in data availability that can be gained from a sensor in geostationary orbit.

Fig. 10 shows the comparison of the timing of maximum T derived from the smoothed SEVIRI VIS06 time series (see big red dots in

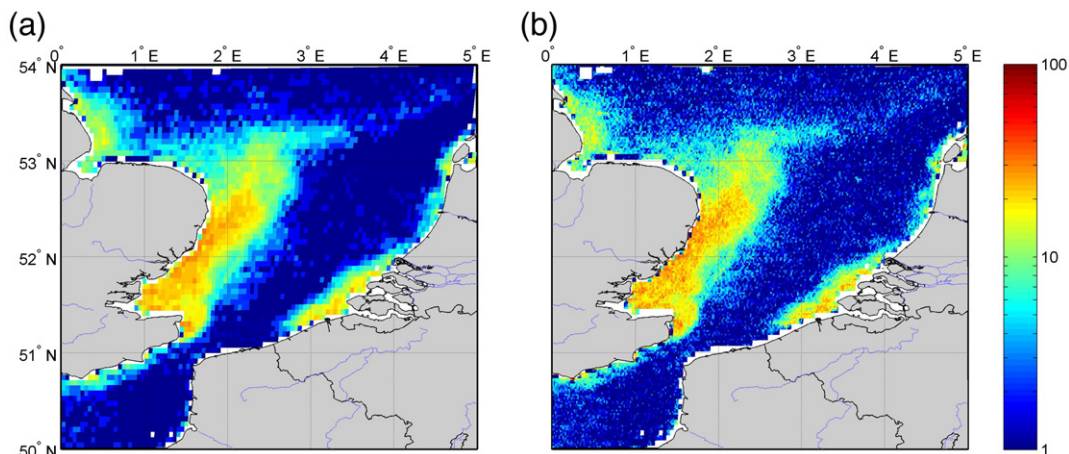


Fig. 6. Turbidity on February 11, 2008 at 13:00 UTC for a subset of the SEVIRI southern North Sea scene on (a) the SEVIRI VIS06 grid with a spatial resolution of $3 \text{ km} \times 6.5 \text{ km}$ and (b) on the HRV grid with a spatial resolution of $1 \text{ km} \times 2 \text{ km}$.

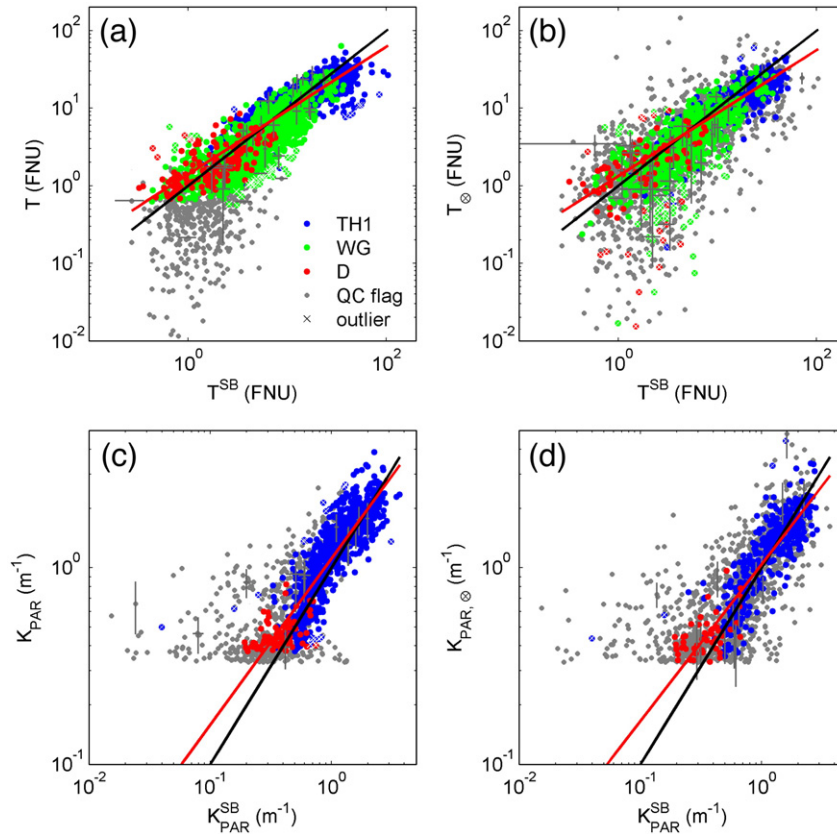


Fig. 7. Scatter plots of SEVIRI vs. SmartBuoy turbidity (T) and light attenuation (K_{PAR}) at TH1, WG, and D for the period 2008–2009 on the low (a, c) and the high (b, d) spatial resolution SEVIRI grids. Regression lines are shown in red (equations and statistics in Table 3), while the 1:1 line is shown in black. Quality flagged observations are shown in grey and correspond to pixels where either the SEVIRI marine reflectances have over 100% uncertainty (a, b, c, d), or low quality PAR measurements (c, d), or low quality PAR measurements (c, d). Error bars are plotted for 1% random observations and denote uncertainties on SmartBuoy and SEVIRI products expressed by Eq. 41 and Eqs. 36 and 39, respectively. Regression outliers are labelled by white crosses.

Figs. 8 and 9) against the timing of maximum T obtained from the SmartBuoys for all available cloud free periods ($n = 49$). In 75% of the cases, the phase difference is less than one hour. On average, the maximum SEVIRI T is reached 11 min before the maximum SmartBuoy T , with a standard error of 1.46 h.

3.3.2. Time series of PAR attenuation

A total of 46 continuous and cloud free SEVIRI/SmartBuoy K_{PAR} time series at TH1 and D longer than 4.5 h were found of which 27 satisfied the selection criteria described in Section 2.7.3. Six randomly selected time series are shown in Fig. 11. Approximately 6-hourly variability is apparent for some time series, although other temporal variability is also apparent. For comparison, data availability from MODIS Aqua, MODIS Terra, and MERIS ENVISAT is also indicated in Fig. 11. Fig. 12 shows the comparison of the timing of maximum

K_{PAR} derived from the smoothed SEVIRI VIS06 time series (see big red dots in Fig. 11) against the timing of maximum K_{PAR} obtained from the SmartBuoys for all available cloud free periods. In 80% of the cases, the phase difference is less than one hour. On average, the maximum SEVIRI K_{PAR} is reached 23 min before the maximum SmartBuoy K_{PAR} , with a standard error of 1.27 h.

4. Discussion

Overall, good correspondence is found between the SEVIRI and SmartBuoy products for both T and K_{PAR} , but with considerable scatter along the 1:1 line as shown in Fig. 7. There are several possible causes for differences between SEVIRI and SmartBuoy data including: small spatial scale variability (point vs. pixel comparison), uncertainties of the SEVIRI atmospheric correction and digitization, design of the

Table 4

Equation and statistics of the least squares cubic log–log regressions between SmartBuoy and SEVIRI T and K_{PAR} products obtained on the SEVIRI low and high (\otimes subscript) spatial resolution grids. The total number of match-ups is given by n_{tot} , of which n_v passed the quality control criteria (see Sections 2.2.1 and 2.2.2 for details), and from which n_x were removed as regression outliers. The correlation coefficient, r , with 95% confidence interval ($r \pm \Delta r$), slope, a , and offset, b , of the regression line are given with their standard errors. The RMSE (units of P), and the 5th, 50th, and 95th percentiles of the prediction error (PE) and the bias are given.

P	n_{tot}	n_v	n_x	r	Δr	$\log_{10} P = a(\pm \Delta a) \log_{10} P^{SB} + b(\pm \Delta b)$				RMSE	PE (%)			Bias (%)		
						a	Δa	b	Δb		5	50	95	5	50	95
T	3068	2598	51	0.933	0.006	0.822	0.009	0.148	0.010	5.795	3	29	80	−65	−14	77
T_{\otimes}	3068	1412	72	0.922	0.009	0.812	0.012	0.126	0.013	5.340	3	32	93	−73	−20	82
K_{PAR}	1492	988	16	0.926	0.008	0.846	0.014	0.047	0.003	0.342	2	18	81	−27	9	81
$K_{PAR, \otimes}$	1492	424	4	0.917	0.015	0.798	0.022	0.018	0.005	0.341	2	19	79	−35	5	79

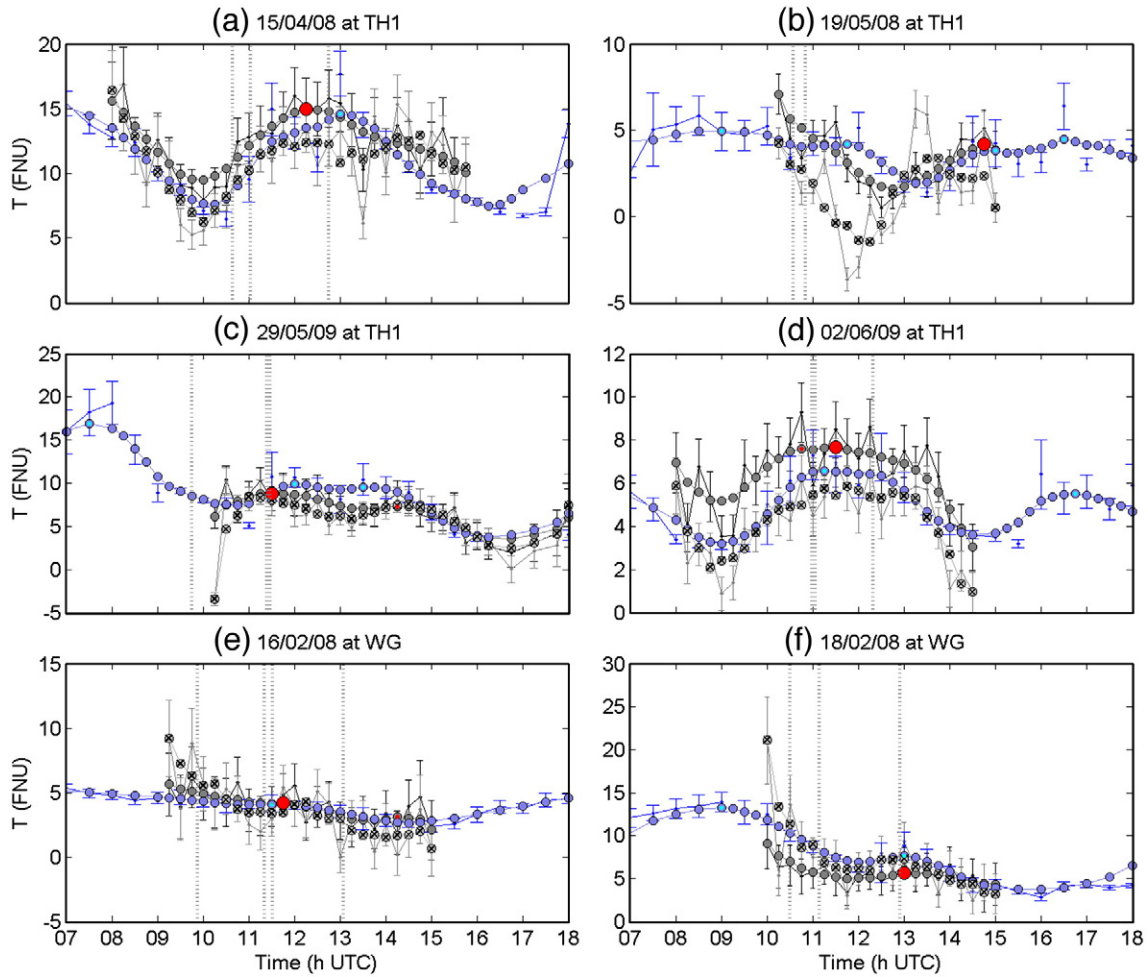


Fig. 8. Randomly selected original and smoothed time series of T obtained from SEVIRI and SmartBuoys. SEVIRI T data from the VIS06 and HRV bands with their uncertainty (see Eq. (36)) are shown by the black and grey error bars, respectively. Temporally smoothed data series for VIS06 (O) and HRV (\otimes) T products are shown in grey, with global (big red dot) and local (small red dots) maxima. SmartBuoy T and its uncertainty is shown by the blue error bars, while the temporally smoothed data series is shown by blue circles with local maxima highlighted in cyan. Grey vertical dotted lines represent data availability from MODIS Aqua/Terra and MERIS ENVISAT.

SEVIRI retrieval algorithms for T and K_{PAR} , and incommensurability between in situ and remotely sensed products.

4.1. Limitations of the atmospheric correction and sensor digitization

The uncertainty estimate on SEVIRI marine reflectance combines uncertainties due to the atmospheric correction assumptions and SEVIRI digitization (see Eq. (33)). Digitization uncertainties are of the order 0.004, as can be seen from Table 3 for a typical sun zenith angle of 40° . This minimum uncertainty on the retrieved marine reflectance corresponds to a turbidity detection limit for SEVIRI of $T=0.9$ FNU after Eq. 35. This explains the location of the majority of the grey dots in Fig. 7(a). Comparison with T^{SB} for these observations is clearly problematic.

While the SEVIRI atmospheric correction in clear waters is limited by the SEVIRI digitization uncertainty, the atmospheric correction is expected to fail in very turbid waters, due to the non-linearity of the VIS06:VIS08 marine reflectance ratio (assumption in Eq. (23)) for very high reflectance (see Fig. 5 in Neukermans et al., 2009). This assumption is only valid for waters with $\rho_w^{0+(0.8)} < 0.011$ and thus $\rho_w^{0+(0.6)} < 0.062$. The effect of this assumption on the atmospheric correction for waters with higher marine reflectance can be understood by studying the normalized bias of the marine reflectance

retrieved by SEVIRI (after Eq. (25) with $\rho_a^{(0.8)} = 0.01$ and simplifications $\gamma = 1 = t_{o,v}^{a(0.8)}$) from the in situ measured marine reflectance $\rho_{w,m}^{0+(0.6)}$:

$$NB = \frac{\rho_w^{0+(0.6)} - \rho_{w,m}^{0+(0.6)}}{\rho_{w,m}^{0+(0.6)}}$$

Fig. 13 shows the relationship between NB and $\rho_{w,m}^{0+(0.6)}$ for a typical range of ε values. For $\varepsilon = 1.02$, $\rho_w^{0+(0.6)}$ is underestimated by about 10% for $\rho_w^{0+(0.6)} = 0.08$ ($T = 34$ FNU), and by over 25% for larger reflectances. This corresponds to an underestimation in T of 18% and 53%, respectively. Taking account of sensor digitization and the limitations due to the σ atmospheric correction assumption, SEVIRI's atmospheric correction is expected to perform optimally for $0.004 < \rho_w^{0+(0.6)} < 0.080$, which corresponds to an optimal T retrieval between 1 and 35 FNU. This may explain why the majority of the observations with T^{SB} above 35 FNU lie below the 1:1 line in Fig. 7(a).

Fig. 14 gives a map of the percentage of observations of $\rho_w^{0+(0.6)}$ in 2008–2009 that lie in the SEVIRI optimal range, i.e. between 0.004 and 0.08×0.9 (where the 0.9 factor accounts for the 10% underestimation when $\rho_w^{0+(0.6)} = 0.08$ shown in Fig. 13). At TH1, 93% of the observations are in the optimal range, whereas at WG and D marine

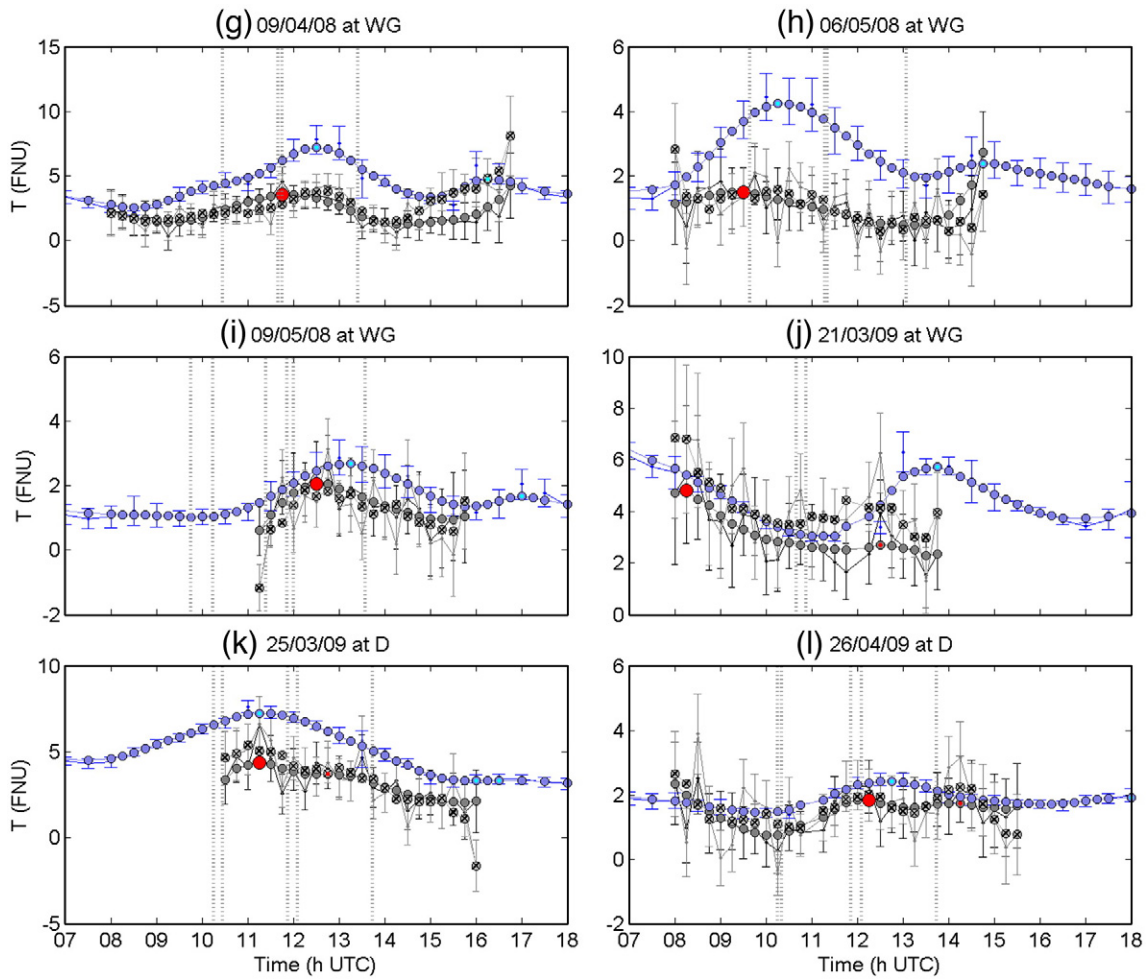


Fig. 9. Continuation of Fig. 8.

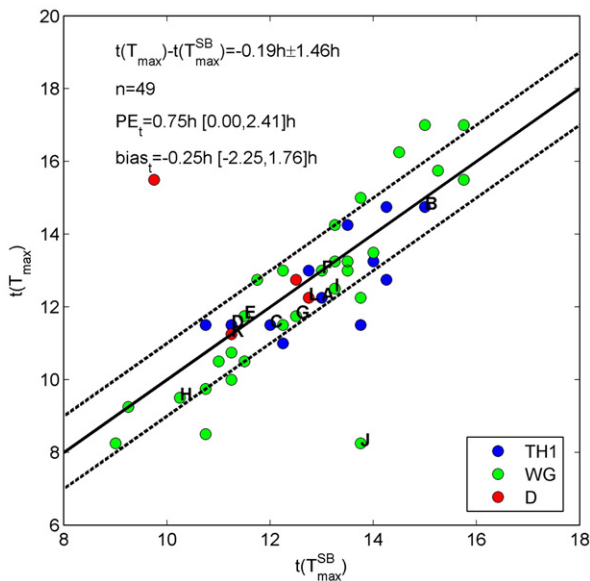


Fig. 10. Scatter plot of the timing of maximum turbidity derived from the SmartBuoys (TH1, WG, and D) and SEVIRI for 49 cloud free time series. The 1:1 line (solid) and 1 h offset lines (dashed) are shown in black. Labels refer to the time series shown in Fig. 8 and Fig. 9. The mean and standard deviation of the phase difference, median and 5th–95th percentile interval for prediction error and bias are also given.

reflectance is optimally retrieved in 65% and 42% of the observations, respectively.

It might be possible to push the upper retrieval limit further by refining the algorithm to have a non-constant σ via an extra iterative loop with σ calculated as a function of $\rho_w^{0+(0.8)}$. However, the issue of non-constant σ in the atmospheric correction is mirrored by limitations of the reflectance model underlying Eq. 35 near its high reflectance asymptote. This “saturation” phenomenon (Bowers et al., 1998) is ideally avoided for ocean colour sensors such as MERIS by using longer wavelengths where pure water absorption is higher (Shen et al., 2010). Unfortunately, for SEVIRI this is not an option due to its low spectral resolution and high digitization/noise uncertainties. SEVIRI’s short wave infrared band (NIR1.6) has been considered previously for aerosol correction, but resulted in even higher atmospheric correction uncertainties due to its very high digitization/noise (see Appendix A of Neukermans et al., 2009).

4.2. Limitations of SEVIRI spatial resolution: pixel vs. point observations

Contrary to our expectations, the improved spatial resolution of SEVIRI products did not improve correspondence with SmartBuoy data. This could be caused by imperfect alignment of the SEVIRI VIS06 and the HRV spatial grids (Seiz et al., 2007), by the spatial heterogeneity of aerosols within each VIS06 grid pixel, or by digitization/noise effects for the HRV band. Removal of SEVIRI observations neighbouring clouds or masked pixels ($t_{a,v}^{(0.6)} < 0.85$) strongly reduced the scatter along the 1:1 line in Fig. 7(b,d).

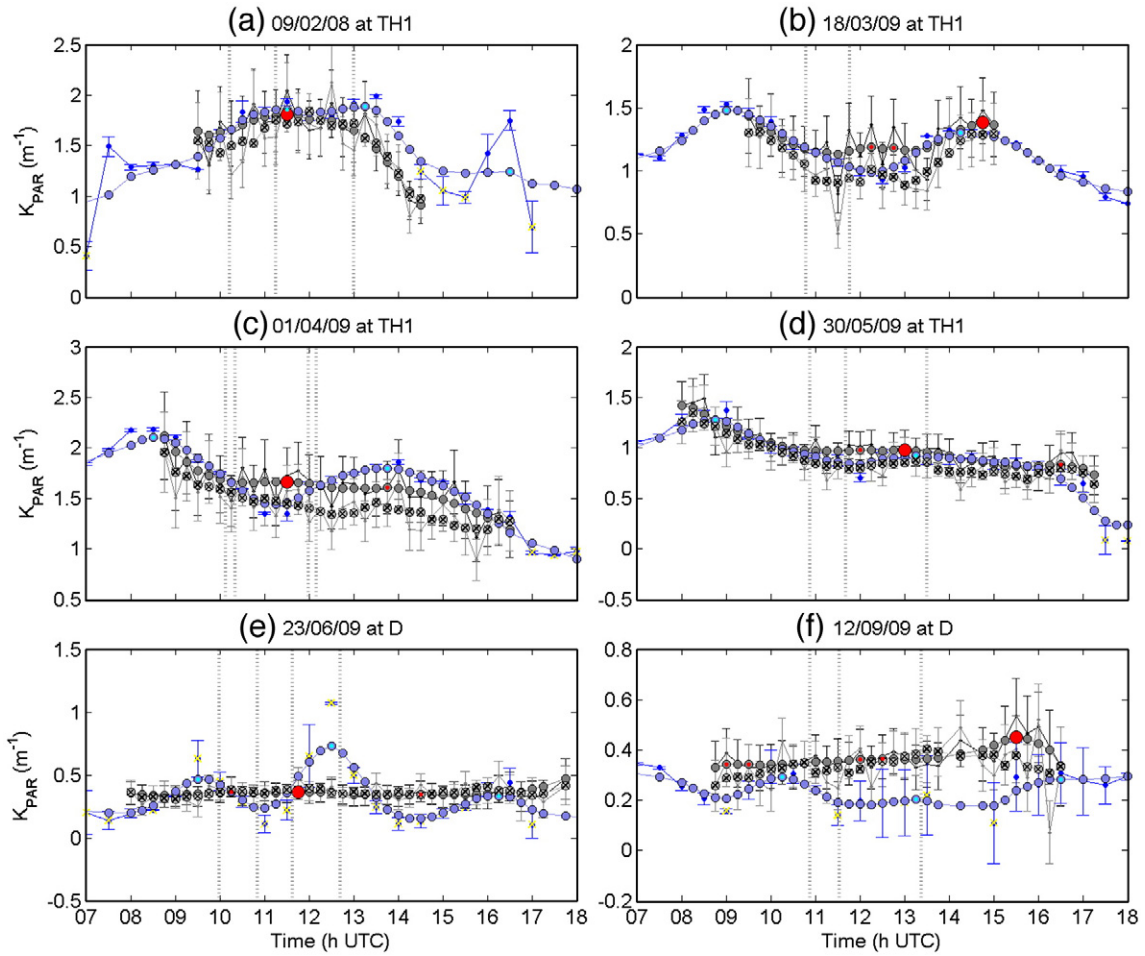


Fig. 11. Six randomly selected original and smoothed time series of K_{PAR} obtained from SEVIRI and SmartBuoys. SEVIRI K_{PAR} data from the VIS06 and HRV bands with their uncertainty (from Eq. (39)) are shown black and grey error bars, respectively. Temporally smoothed data series for VIS06 and HRV (\otimes) K_{PAR} products are shown in grey, with global (big red dot) and local (small red dots) maxima. SmartBuoy K_{PAR} and uncertainties (from Eq. (41)) are shown by the blue circles, while the temporally smoothed data series are shown by blue circles with local maxima highlighted in cyan. Grey vertical dotted lines represent data availability from MODIS Aqua/Terra and MERIS ENVISAT. The yellow crosses indicate quality flagged K_{PAR} SmartBuoy data (from Eq. (42)).

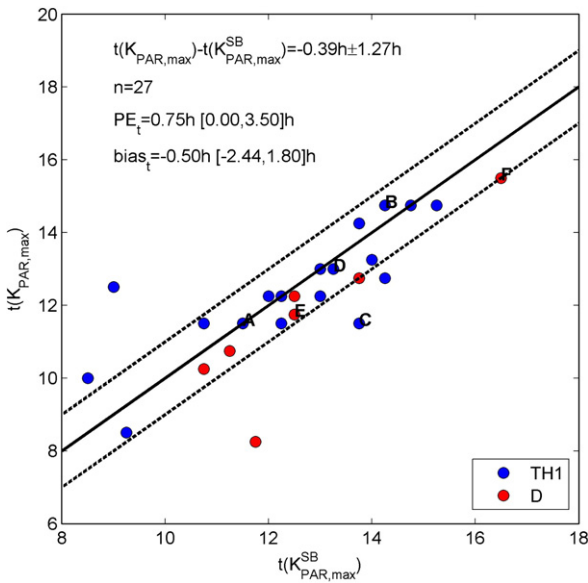


Fig. 12. Scatter plot of the timing of maximum PAR attenuation derived from the SmartBuoys (TH1 and D) and SEVIRI during 27 cloud free periods. The 1:1 line (solid) and 1 h offset lines (dashed) are shown in black. Labels refer to the time series shown in Fig. 11. The mean and standard deviation of the phase difference, median and 5th–95th percentile interval for prediction error and bias are also given.

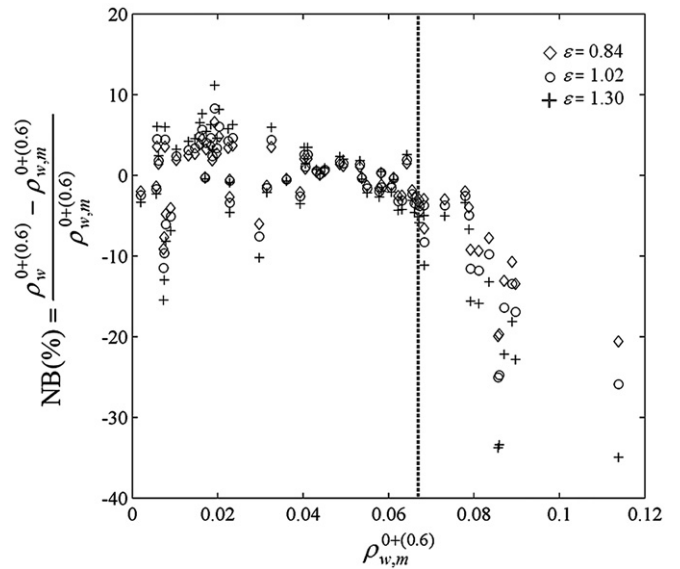


Fig. 13. Effect of the atmospheric correction assumption of constant σ on the retrieval of $\rho_w^{0+(0.6)}$; normalized bias of $\rho_w^{0+(0.6)}$ obtained from SEVIRI from the true marine reflectance for a typical range of ϵ values, with $\rho_a^{(0.8)} = 0.01$ and simplifications $\gamma = 1 = t_{a,v}^{(0.8)}$. The dashed line demarcates the reflectance region where σ was calibrated.

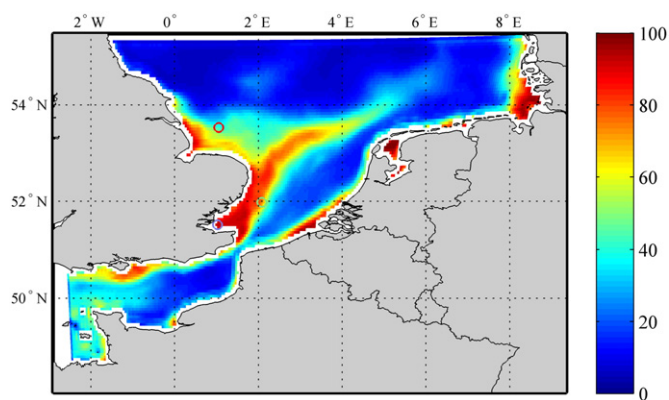


Fig. 14. Map of percentage of total SEVIRI observations in 2008–2009 where SEVIRI marine reflectance was in the optimal range, i.e. $0.004 < \rho_w^{0+(0.6)} < 0.072$. Circles mark the location of SmartBuoys at TH1 (blue), WG (green), and D (red). Data with less than 100 valid observations were masked.

4.3. Limitations of the SEVIRI retrieval algorithms

Analogous to the assumption of constant [SPM]-specific particulate backscattering coefficient ($=b_{dp}:[SPM]$) in the single band [SPM] retrieval algorithm of Nechad et al. (2010), the T retrieval algorithm (Nechad et al., 2009 in Eq. 35) is based on the assumption that the T -specific backscattering coefficient ($=b_{dp}:T$) is constant. Like $b_{dp}:[SPM]$, $b_{dp}:T$ is relatively well constrained with variability of a factor 3 (see Appendix A and Neukermans et al., 2012). Variability in $b_{dp}:T$ is best explained by variations in particle composition (see Appendix A). Significant, but weaker, correlations with particle size and density were also found, however. This implies that for a water mass of fixed turbidity, changes in particle composition from mainly organic to mainly inorganic will lead to a higher remotely sensed T . Particle composition could vary on time scales of a few hours, for example due to tidal resuspension of inorganic bottom sediments (Thompson et al., 2011).

The K_{PAR} retrieval algorithm is based on the optical model of Devlin et al. (2008), identifying suspended particles as the main source of light attenuation (K_{PAR} is proportional to [SPM], see Eq. 37). This one parameter model was found by Devlin et al. (2008) to represent most of the variability in K_{PAR} that was measured at a variety of North Sea stations and gives good performance here for the more turbid waters. It is ideally suited to the limited spectral resolution of the SEVIRI sensor which is essentially limited to the retrieval of [SPM] (and covarying parameters) only. See also Stumpf et al. (1999) for a study with the spectrally similar polar-orbiting AVHRR sensor. Expressing K_{PAR} as a linear function of [SPM] is clearly a gross simplification because K_{PAR} can be affected by variability of many factors including: concentration of coloured dissolved organic matter (CDOM, Kratzer & Tett, 2009), phytoplankton (expressed via Chl a concentration), size, shape and composition of suspended particles, the average cosine of downwelling irradiance (or sun zenith angle), the spectral composition of incident irradiance, and the invalidity of the Lambert–Beer “law” (Gordon, 1989). Any of the first three factors could explain the apparent difference in performance of the SEVIRI K_{PAR} product during clear water periods at TH1 (SEVIRI underestimates) and D (SEVIRI overestimates). The single parameter K_{PAR} model is expected to perform poorly in clearer waters with varying concentrations of CDOM and Chl a , because their contribution is represented by a constant offset (see Eq. 37). In the North Sea, CDOM has a mainly terrestrial origin (Foden et al., 2008) and decreases with salinity (e.g., Astoreca et al., 2009). Salinity data recorded by the SmartBuoys in 2008–2009 give average values of 34.14 ± 0.68 PSU and 34.54 ± 0.17 PSU at TH1 and D, respectively, which corresponds to observations in Fig. 7(c,d) of higher K_{PAR} at TH1 than at D in clear waters. It

is, however, beyond the scope of this paper and beyond the scope of the SEVIRI sensor to resolve the question of CDOM impact on K_{PAR} , although improvement of the SEVIRI K_{PAR} model might be achievable by integrating lower frequency information on CDOM and phytoplankton (or euphotic depth) from suitably designed polar-orbiting ocean colour sensors such as MODIS or MERIS.

4.4. Incommensurability between in situ and remotely sensed products

4.4.1. Remotely sensed vs. in situ T

The T retrieval algorithm in Eq. 35 is calibrated using in situ measurements of marine reflectance and measurements of side scattering (90° scattering angle) at a wavelength of 860 nm (Hach 2100P turbidity meter), whereas the SmartBuoy T is measured with a Seapoint turbidity meter, which records particulate scattering at a wavelength of 880 nm between 15° and 150° . Both instruments are calibrated with Formazine suspensions and give output relative to Formazine in FNU. Despite both turbidity instruments being calibrated with standard Formazine suspensions, their response in natural waters will be different because of their different angular configuration (Roesler & Boss, 2007). The wide solid angle of the Seapoint turbidity meter also includes forward scattering and increases the instrument's sensitivity to particle size compared to instruments with narrow solid angles in the back direction such as the Hach 2100P turbidimeter or D&A Tech optical backscatter instruments (OBS-3, FOBS-7, see Downing, 2006 for a comprehensive overview of instrument specifications and sensitivity to bulk particle characteristics). A factor 2 variability between SEVIRI T (which is proportional to the particulate backscattering coefficient, b_{dp} , in the linear regime of the SEVIRI T retrieval algorithm) and Seapoint T was found (Neukermans, 2012) using in situ measurements of the volume scattering function with the WET Labs MASCOT instrument (Sullivan & Twardowski, 2009; Twardowski et al., 2012). This variability is caused by changes in particle size, shape, and composition, which are known to occur on time scales of a few hours (Verney et al., 2011).

4.4.2. Remotely sensed vs. in situ K_{PAR}

Differences between remotely sensed K_{PAR} and in situ K_{PAR} can be caused by differences in the thickness and depth of the water layer considered for deriving K_{PAR} . The SmartBuoy K_{PAR} is obtained from PAR measurements at 1 m and 2 m depth, while the thickness of the remotely sensed layer varies with water clarity and with the wavelength of the light considered. For a vertically homogenous water column, approximately 90% of the marine reflectance at a given wavelength is derived from a layer between the surface and depth K_d^{-1} (Gordon & McCluney, 1975). From inversion of SmartBuoy K_{PAR} , this results in K_{PAR} remote sensing contributions of a layer of water of $3 \text{ m} \pm 1 \text{ m}$ deep at D and of $1.1 \text{ m} \pm 1.0 \text{ m}$ at TH1, on average. Although K_{PAR} may be depth dependent (Lee, 2009), an average PAR attenuation coefficient, \bar{K}_{PAR} , is usually derived from a water layer extending from the surface down to the euphotic depth, where PAR has dropped to 1% of its surface value (Kirk, 1996, 2003; Morel, 1988). Therefore, the SEVIRI derived K_{PAR} represents the mean PAR attenuation in the euphotic zone.

4.5. Perspectives for the design of future geostationary sensors and synergy with polar-orbiting sensors

It is shown here that the SEVIRI sensor can be used to estimate T and K_{PAR} in the turbid waters of the southern North Sea and their tidal variability for the first time from space. However, this meteorological sensor was not designed for ocean remote sensing and hence its ocean application has a number of limitations, as shown in this study. Future geostationary ocean colour sensors should have (i) better spectral resolution, e.g. 5–8 visible/near infrared bands for open ocean chlorophyll retrieval and more for applications in coastal

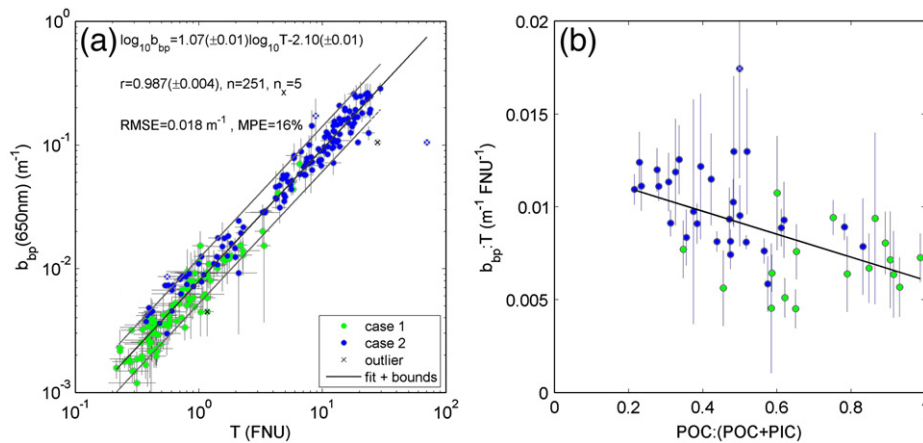


Fig. 15. (a) Relationship between the particulate backscattering coefficient, b_{bp} ($\lambda = 650$ nm), and turbidity in clear (case 1) and turbid (case 2) waters. The regression line with its 90% confidence bounds in log–log scale and statistics are shown (MPE = median PE). (b) Variability of T -specific b_{bp} as a function of particle composition. The fitted regression and statistics can be found in Table 5. See also Neukermans et al. (2012) for details on in situ measurements and data treatment.

waters (IOCCG, 2000), instead of two for SEVIRI (VIS06 and VIS08), (ii) finer digitization and better signal to noise ratio for observation of dark targets like the ocean, and (iii) higher spatial resolution, possibly by the use of mixed resolution broad/narrow bands (mimicked here by the VIS06/HRV combination).

For Chl a estimation, the atmospheric correction for blue bands will be particularly difficult, especially for the high air masses encountered at high latitudes by geostationary remote sensing. The use of a geosynchronous orbit (IOCCG, 2012) may mitigate this slightly but at the cost of a varying viewing geometry.

While the current paper demonstrates remote sensing of tidal variability associated with [SPM], many other high frequency processes become potentially amenable to remote sensing by a geostationary ocean colour sensor, including diurnal variability of photosynthetic processes, bidirectionality of aerosol or hydrosol particulate scattering (via sun variation in day, for stable conditions), diurnal migration of certain algal species, etc (IOCCG, 2012). These new processes add to the obvious practical advantage of better coverage from high temporal frequency data in regions or periods of scattered clouds. Finally, it is probable that entirely new ways will be found to process high frequency ocean colour data, where the current pixel-by-pixel approach may be supplemented by consideration of temporal coherency of data in analogy to approaches already explored in atmospheric remote sensing (Kaufman et al., 1997).

The synergy between polar-orbiting and geostationary sensors still needs to be investigated with the aim of exploiting the advantages of each orbit: the higher spatial resolution and better atmospheric correction of polar-orbiters, especially for high latitudes and the higher frequency of geostationary-orbiters. In the context of the current paper, a potential synergy would be to use background information on CDOM and [Chl a] and higher spatial resolution

information on [SPM] from polar-orbiters, modulated by the high frequency variability of [SPM] observed here by SEVIRI. This could further be combined with a geostatistical cloud-filling and outlier detection approach, similar to that of (Sirjacobs et al., 2011), to give unprecedented details of spatio-temporal variability of PAR attenuation for the forcing of ecosystem models.

5. Conclusion

This study successfully extended the methodology developed by Neukermans et al. (2009) for mapping of suspended matter in the southern North Sea from the SEVIRI sensor to the mapping of turbidity, T , and vertical attenuation, K_{PAR} , of photosynthetically active radiation (PAR). Based on numerous match-ups from a two year archive of SEVIRI imagery and half-hourly T and K_{PAR} data from a system of moored buoys (SmartBuoys), good correspondence was found, with 80% of SEVIRI derived T and K_{PAR} being within 53% and 39% of SmartBuoy T and K_{PAR} , respectively. The previous atmospheric correction was improved and the uncertainties on marine reflectance due to digitization were considered. Also, the spatial resolution of the SEVIRI products is improved from $3 \text{ km} \times 6.5 \text{ km}$ to $1 \text{ km} \times 2 \text{ km}$, becoming comparable to the spatial resolution of the polar-orbiting MODIS ocean colour satellite. During cloud free periods diurnal variability of T and K_{PAR} is detected by SEVIRI and comparison with SmartBuoy time series shows that the signals are in phase with an average difference in the timing of the maximum T and K_{PAR} of 11 min and 23 min, respectively. This diurnal variability is now detected from remote sensing for the first time, offering new opportunities for improving ecosystem models and monitoring of turbidity.

The limitations of the methodology have also been clearly identified and include: the limited spectral resolution of SEVIRI, the limited

Table 5
Correlations and regression analysis of turbidity-specific backscattering vs. mean particle diameter (D_A), mean apparent density (ρ_a), and particle composition. ns: not significant (i.e., $p > 0.05$), n_o is the number of observations, n_x is the number of outliers removed as described in Neukermans et al. (2012).

x	Case	n_o	n_x	r	Equation (units: $\text{m}^{-1} \text{FNU}^{-1}$), RMSE, MPE (%)
ρ_a (kg L^{-1})	1	35	0	0.43 ± 0.34	–
	2	72	2	ns	–
	1 + 2	107	3	$0.27 \pm 0.17^*$	$0.013(\pm 0.002) x + 0.0052(\pm 0.0005), 0.0029, 19$
D_A (μm)	1	35	0	ns	–
	2	72	3	$0.59 \pm 0.17^*$	$0.00006(\pm 0.00002) x + 0.0075(\pm 0.0004), 0.0019, 11$
	1 + 2	107	4	$0.32 \pm 0.17^*$	$0.00004(\pm 0.00002) x + 0.0077(\pm 0.0004), 0.0023, 15$
POC: (POC + PIC)	1	17	0	ns	–
	2	30	1	$-0.52 \pm 0.22^*$	$-0.007(\pm 0.002) x + 0.013(\pm 0.001), 0.0017, 12$
	1 + 2	47	1	$-0.57 \pm 0.17^*$	$-0.006(\pm 0.001) x + 0.012(\pm 0.001), 0.0019, 14$

* $p < 0.001$.

digitization of SEVIRI, limitations in usage of the HRV band, the use of a single parameter model for K_{PAR} as well as different definitions for the remotely sensed T and K_{PAR} products and the in situ measurements used to validate them. In fact, when considering all these difficulties it is perhaps surprising that any useful marine information at all can be retrieved from a meteorological sensor designed to look at clouds, a much brighter target. However, the information on tidal variability of T and K_{PAR} presented here is clearly a significant improvement on the aliased information that is provided by MODIS and MERIS and that is already being used in both monitoring and modelling applications. The present study provides a glimpse of what will become possible when dedicated geostationary ocean colour sensors become operational and provides some first hints on the methodological challenges and opportunities that they will raise.

Acknowledgements

This research was supported by the BELCOLOUR-2 and GEOCOLOUR projects, funded by the STEREO programme of the Belgian Science Policy Office under contracts SR/00/104 and SR/00/139, respectively. Many thanks to Nicholas Clerbaux of the Royal Meteorological Institute of Belgium for providing SEVIRI data. Thanks to Quinten Vanhellemont for MODIS time series extraction. The crew of the Belgica research vessel is thanked for their kind help during sea campaigns. MUMM's chemistry laboratory is acknowledged for the analysis of [SPM] and [Chl *a*] data. The SmartBuoy data was collected in the Defra-funded projects SLA25 and E5304. Backscattering data presented in Appendix A was kindly processed by Xavier Mériaux at ULCO-LOG. The first author is involved in a MUMM-ULCO collaborative Ph.D. research project. Her promoter, Hubert Loisel, is thanked for his support.

Appendix A. Variability of turbidity-specific backscattering

The single band retrieval algorithms for T (Nechad et al., 2009) and SPM (Nechad et al., 2010) are based on the assumption that T - and SPM-specific particulate backscattering coefficients (b_{bp}), respectively, are constant. In analogy with the study of natural variability of SPM-specific backscattering of Neukermans et al. (2012), the variability of T -specific particulate backscattering ($=b_{bp}T$) is investigated using the same dataset and methodology. Fig. 15(a) shows a scatter plot of all available in situ T and b_{bp} data ($n = 251$). T and b_{bp} are well correlated with a correlation coefficient of 0.987 ± 0.004 and the fitted log–log regression has a median prediction error (MPE) of 16%. Results of the correlation and regression analysis of $b_{bp}T$ vs. mean particle diameter (D_A), mean apparent density (ρ_a), and particle composition on the same data subset as in Neukermans et al. (2012) are shown in Table 5. The median b_{bp} to T ratio is 0.0089, with 90% of the ratios between 0.0045 and $0.0135 \text{ m}^{-1} \text{ FNU}^{-1}$, giving variability in $b_{bp}T$ of a factor 3. A similarly small range of variability in b_{bp} :SPM was found (a factor 3–4). For pooled clear (case 1) and turbid (case 2) waters, statistically significant correlations are found between $b_{bp}T$ and ρ_a , D_A , and particle composition (expressed as the ratio of particulate organic carbon concentration, POC, to total carbon concentration, POC + PIC). The highest amount of variability (32%) is explained by the latter, with inorganic particles having $b_{bp}T$ coefficients that are about 2 times higher than for organic particles (see Fig. 15(b)).

References

- Alvain, S., Moulin, C., Dandonneau, Y., & Loisel, H. (2008). Seasonal distribution and succession of dominant phytoplankton groups in the global ocean: A satellite view. *Global Biogeochemical Cycles*, 22, GB3001, <http://dx.doi.org/10.1029/2007GB003154>.
- Antoine, D., et al. (2011). HOCI: A hosted ocean colour imager on board EDRS-C. *Proposal in answer to ESA Call for interest on in-orbit validation of payloads hosted on-board telecommunication satellites* Ref: EB.LT.TB.11.00002.
- Astoreca, R., Rousseau, V., & Lancelot, C. (2009). Coloured Dissolved Organic Matter (CDOM) in Southern North Sea waters: Optical characterization and possible origin. *Estuarine Coastal and Shelf Sea Science*, 85, 633–640.
- Bowers, D. G., Boudjelas, S., & Harker, G. E. L. (1998). The distribution of fine suspended sediments in the surface waters of the Irish Sea and its relation to tidal stirring. *International Journal of Remote Sensing*, 19, 2789–2805.
- Christian, D., & Sheng, Y. P. (2003). Relative influence of various water quality parameters on light attenuation in Indian River Lagoon. *Estuarine Coastal and Shelf Science*, 57, 961–971.
- Deng, S. (2009). Findextrema.m MATLAB script to find indices of local extrema (minima, maxima) and zero-crossings. Source: <http://www.mathworks.com/matlabcentral/fileexchange/24306-findextrema>
- Devlin, M. J., Barry, J., Mills, D. K., Gowen, R. J., Foden, J., Sivyver, D., et al. (2008). Relationships between suspended particulate material, light attenuation and Secchi depth in UK marine waters. *Estuarine, Coastal and Shelf Science*, 79, 429–439.
- Downing, J. (2006). Twenty-five years with OBS sensors: The good, the bad and the ugly. *Continental Shelf Research*, 26, 2299–2318.
- Eisma, D., & Irion, G. (1988). Suspended matter and sediment transport. In W. Salomons, B. L. Bayne, E. K. Duursma, & U. Förstner (Eds.), *Pollution of the North Sea: An assessment* (pp. 20–33). Berlin: Springer.
- Faure, F., Coste, P., & Kang, G. (2008). The GOCI instrument on COMS mission – The first geostationary ocean color imager. *Proceedings of the International Conference on Space Optics (ICSO), 14–17 October 2008, Toulouse, France*.
- Foden, J., Sivyver, D., Mills, D., & Devlin, M. J. (2008). Spatial and temporal distribution of chromophoric dissolved organic matter (CDOM) fluorescence and its contribution to light attenuation in UK water bodies. *Estuarine, Coastal and Shelf Science*, 79, 707–717.
- Gordon, H. R. (1989). Can the Lambert–Beer Law be applied to the diffuse attenuation coefficient of ocean water? *Limnology and Oceanography*, 34, 1389–1409.
- Gordon, H. R., & McCluney, W. R. (1975). Estimation of depth of sunlight penetration in sea for remote-sensing. *Applied Optics*, 14, 413–416.
- Ham, S. H., & Sohn, B. J. (2010). Assessment of the calibration performance of satellite visible channels using cloud targets: Application to Meteosat-8/9 and MTSAT-1R. *Atmospheric Chemistry and Physics*, 10, 1131–1149.
- International Ocean Colour Coordinating Group (IOCCG) (2000). Remote sensing of ocean colour in coastal, and other optically-complex waters. In S. Sathyendranath (Ed.), *Reports of the International Ocean Colour Coordinating Group, No. 3, IOCCG, Dartmouth, Canada*.
- International Ocean Colour Coordinating Group (IOCCG) (2012). Ocean colour observations from a geostationary orbit. In D. Antoine (Ed.), *Reports of the International Ocean Colour Coordinating Group, No. 12, IOCCG, Dartmouth, Canada*.
- International Organization for Standardization (ISO) (1995). Guide to the expression of uncertainty in measurement. ISO 1995 (pp. 101).
- International Organization for Standardization (ISO) (1999). Water quality – Determination of turbidity. ISO 1999 (pp. 7027).
- Kaufman, Y. J., Tanré, D., Gordon, H. R., Nakajima, T., Lenoble, J., Fouin, R., et al. (1997). Passive remote sensing of tropospheric aerosol and atmospheric correction for the aerosol effect. *Journal of Geophysical Research*, 102, 16,815–16,830.
- Kirk, J. T. O. (1996). *Light and photosynthesis in aquatic ecosystems*. Cambridge University Press.
- Kirk, J. T. O. (2003). The vertical attenuation of irradiance as a function of the optical properties of the water. *Limnology and Oceanography*, 48, 9–17.
- Kratzer, S., & Tett, P. (2009). Using bio-optics to investigate the extent of coastal waters: A Swedish case study. *Hydrobiologia*, 629, 169–186.
- Lacroix, G., Park, Y., Ruddick, K., & Lancelot, C. (2007). Spatial and interannual variability of the spring phytoplankton bloom in the North Sea investigated by modelling and remote sensing. *Proceedings of the 6th European Conference on Ecological Modelling (ECEM'07)*.
- Lawson, S. E., Wiberg, P. L., Mcglathery, K. J., & Fugate, D. C. (2007). Wind-driven sediment suspension controls light availability in a shallow coastal lagoon. *Estuaries and Coasts*, 30, 102–112.
- Lee, Z. (2009). KPAR: An optical property associated with ambiguous values. *Journal of Lake Sciences*, 21, 159–164.
- Loisel, H., Nicolas, J. -M., Sciandra, A., Stramski, D., & Poteau, A. (2006). Spectral dependency of optical backscattering by marine particles from satellite remote sensing of the global ocean. *Journal of Geophysical Research*, 111, C09024, <http://dx.doi.org/10.1029/2005JC003367>.
- Mazeran, C., & Meskini, N. (2008). Mission Couleurd l'Océan Géostationnaire: Caractérisation de la géométrie, gain en couverture, impact d'instabilités instrumentales. *CNES-044-R650-RF-v1*.
- McClain, C. R. (2009). A decade of satellite ocean color observations. *Annual Review of Marine Science*, 1, 19–42, <http://dx.doi.org/10.1146/annurev.marine.010908.163650>.
- Mills, D. K., Laane, R. W. P. M., Rees, J. M., Loeff, M. R. V. D., Suylen, J. M., Pearce, D. J., et al. (2003). Smartbuoy: A marine environmental monitoring buoy with a difference. In H. Dahlin, N. C. Flemming, K. Nittis, & S. E. Peterson (Eds.), *Building the European Capacity in Operational Oceanography, Proc. Third International Conference on EuroGOOS. Elsevier Oceanography Series Publication series*, 19, (pp. 311–316).
- Morel, A. (1988). Optical modelling of the upper ocean in relation to its biogenous matter content (case 1 waters). *Journal of Geophysical Research*, 93, 10,749–10,768.
- National Research Council (NRC) (2007). *Earth science and applications from space: National imperatives for the next decade and beyond*. Washington, D.C.: The National Academies Press.
- Nechad, B., Ruddick, K. G., & Neukermans, G. (2009). Calibration and validation of a generic multisensor algorithm for mapping of turbidity in coastal waters. *SPIE European International Symposium on Remote Sensing*, 7473.
- Nechad, B., Ruddick, K. G., & Park, Y. (2010). Calibration and validation of a generic multisensor algorithm for mapping of total suspended matter in turbid waters. *Remote Sensing of Environment*, 114, 854–866.

- Neukermans, G. 2012. Optical in situ and geostationary satellite-borne observations of suspended particles in coastal waters. Ph.D. dissertation. Université du Littoral - Côte d'Opale, Wimereux, France. p. 210. Academic and Scientific Publishers, Ravensteingalerij 28, 1000 Brussels, Belgium. ISBN 978 90 7028 949 2.
- Neukermans, G., Loisel, H., Meriaux, X., Astoreca, R., & McKee, D. (2012). In situ variability of mass-specific beam attenuation and backscattering of marine particles with respect to particle size, density, and composition. *Limnology and Oceanography*, 57, 124–144, <http://dx.doi.org/10.4319/lo.2011.4357.4311.0124>.
- Neukermans, G., Ruddick, K., Bernard, E., Ramon, D., Nechad, B., & Deschamps, P. -Y. (2009). Mapping total suspended matter from geostationary satellites: A feasibility study with SEVIRI in the Southern North Sea. *Optics Express*, 17, 14,029–14,052.
- Painting, S. J., Devlin, M. J., Malcolm, S. J., Parker, E. R., Mills, D. K., Mills, C., et al. (2007). Assessing the impact of nutrient enrichment in estuaries: Susceptibility to eutrophication. *Marine Pollution Bulletin*, 55, 74–90.
- Roesler, C. S., & Boss, E. (2007). In situ measurement of the inherent optical properties (IOPs) and potential for harmful algal bloom (HAB) detection and coastal ecosystem observations. In M. Babin, C. Roesler, & J. Cullen (Eds.), *Real-time coastal observing systems for ecosystem dynamics and harmful algal blooms*. : UNESCO.
- Ruddick, K. G., De Cauwer, V., Park, Y., & Moore, G. (2006). Seaborne measurements of near infrared water-leaving reflectance – The similarity spectrum for turbid waters. *Limnology and Oceanography*, 51, 1167–1179.
- Seiz, G., Tjemkes, S., & Watts, P. (2007). Multiview cloud-top height and wind retrieval with photogrammetric methods: Application to Meteosat-8 HRV observations. *Journal of Applied Meteorology and Climatology*, 46, 1182–1195, <http://dx.doi.org/10.1175/JAM2532.1>.
- Shen, F., Verhoef, W., Zhou, Y. X., Salama, M. S., & Liu, X. L. (2010). Satellite estimates of wide-range suspended sediment concentrations in Changjiang (Yangtze) estuary using MERIS data. *Estuaries Coasts*, 33(6), 1420–1429.
- Sirjacobs, D., Alvera-Azcárate, A., Barth, A., Lacroix, G., Park, Y., Nechad, B., et al. (2011). Cloud filling of ocean color and sea surface temperature remote sensing products over the Southern North Sea by the Data Interpolating Empirical Orthogonal Functions methodology. *Journal of Sea Research*, 65, 114–130.
- Stramski, D., Reynolds, R. A., Kahru, M., & Mitchell, B. G. (1999). Estimation of particulate organic carbon in the ocean from satellite remote sensing. *Science*, 285, 239–242.
- Stumpf, R. P., Culver, M. E., Tester, P. A., Tomlinson, M., Kirkpatrick, G. J., Pederson, B. A., et al. (2003). Monitoring *Karenia brevis* blooms in the Gulf of Mexico using satellite ocean color imagery and other data. *Harmful Algae*, 2, 147–160.
- Stumpf, R. P., Frayer, M. L., Durako, M. J., & Brock, J. C. (1999). Variations in water clarity and bottom albedo in Florida Bay from 1985 to 1997. *Estuaries*, 22, 431–444.
- Stumpf, R. P., Gelfenbaum, G., & Pennock, J. R. (1993). Wind and tidal forcing of a buoyant plume, Mobile Bay, Alabama. *Continental Shelf Research*, 13, 1281–1301.
- Sullivan, J. M., & Twardowski, M. S. (2009). Angular shape of the oceanic particulate volume scattering function in the backward direction. *Applied Optics*, 48, 6811–6819.
- Thompson, C. E. L., Couceiro, F., Fones, G. R., Helsby, R., Amos, C. L., Black, K., et al. (2011). In situ flume measurements of resuspension in the North Sea. *Estuarine Coastal and Shelf Science*, 94, 77–88.
- Thuillier, G., Herse, M., Labs, D., Foujols, T., Peetermans, W., Gillotay, D., et al. (2003). The solar spectral irradiance from 200 to 2400 nm as measured by the SOLSPEC spectrometer from the ATLAS and EURECA missions. *Solar Physics*, 214, 1–22.
- Tomlinson, M. C., Stumpf, R. P., Ransibrahmanakul, V., Truby, E. W., Kirkpatrick, G. J., Pederson, B. A., et al. (2004). Evaluation of the use of SeaWiFS imagery for detecting *Karenia brevis* harmful algal blooms in the eastern Gulf of Mexico. *Remote Sensing of Environment*, 91, 293–303.
- Twardowski, M., et al. (2012). The optical volume scattering function in a surf zone inverted to derive sediment and bubble particle subpopulations. *Journal of Geophysical Research*, 117, <http://dx.doi.org/10.1029/2011JC007347>.
- Vantrepotte, V., Loisel, H., Melin, F., Desailly, D., & Duforet-Gaurier, L. (2011). Global particulate matter pool temporal variability over the SeaWiFS period (1997–2007). *Geophysical Research Letters*, 38, L02605, <http://dx.doi.org/10.1029/2010GL046167>.
- Verney, R., Lafite, R., Brun-Cottan, J. C., & Le Hir, P. (2011). Behaviour of a flocculation during a tidal cycle: Laboratory experiments and numerical modelling. *Continental Shelf Research*, 31, S64–S83.
- Woodruff, D. L., Stumpf, R. P., Scope, J. A., & Paerl, H. W. (1999). Remote estimation of water clarity in optically complex estuarine waters. *Remote Sensing of Environment*, 68, 41–52.
- Xu, J., Hood, R. R., & Chao, S. -Y. (2005). A simple empirical optical model for simulating light attenuation variability in a partially mixed estuary. *Estuaries*, 28, 572–580.